Master's Thesis of Engineering

Neuromorphic Computing based on Photon−Magnon Coupling

광−마그논 상호작용에 기반한 뉴로모픽 컴퓨팅

August 2021

Graduate School of Engineering
Seoul National University
Materials Science and Engineering Major

Loïc Millet

i

Neuromorphic Computing based on Photon–Magnon Coupling

광–마그논 상호작용에 기반한 뉴로모픽 컴퓨팅

지도교수 김 상 국

이 논문을 공학석사 학위논문으로 제출함

2021 년 07 월

서울대학교 대학원

재료공학부

Loïc Millet

Loïc Millet의 석사학위 논문을 인준함

2021 년 07 월

위 원 장 _____황 철 성_____

부위원장 _____김 상 국_____

위 원 _____김 상 법_____

Abstract

Loïc Millet

Department of Materials Science and Engineering

The Graduate School

Seoul National University

Neuromorphic computing is a brain-inspired computing paradigm to outperform conventional computing on specific tasks. In particular, reservoir computing is a form of neuromorphic computing that uses a recurrent and randomly interconnected network of non-linear neurons, called a reservoir, to perform classification tasks. To improve further neuromorphic computing efficiency, spintronics-based neuromorphic computing devices are intensively studied. As opposed to conventional CMOS systems emulating neurons and synapses properties, neuromorphic device research aims at creating intrinsically similar devices.

In this work, photon-magnon coupling in a 2D geometry hybrid was successfully used to create a neuron performing waveform recognition in the reservoir computing paradigm. The hybrid system consists of an Inverted Split-Ring Resonator (ISRR) and an Yttrium Iron Garnet (YIG) film. The photon-magnon coupled-

mode properties or Cavity Magnon Polariton (CMP) properties were used as neuron outputs while the waveforms were encoded in a static and uniform magnetic field. High experimental success rates obtained from the CMP mode frequency, S_{21} parameter magnitude and phase demonstrate for the first-time photon-magnon coupling usability for classification tasks. This demonstration is a first step towards realizing more complex tasks and networks relying on photon-magnon coupling in hybrid systems.

Additionally, the concept of a second task relying on a different neuromorphic computing scheme is presented. As demonstrated by pioneering work on Spin Torque Nano-Oscillators (STNO), the synchronization between an oscillator emulating a collection of neurons and an external frequency encoding input data allows computing in a bio-inspired way. This concept has been used to perform vowel recognition, and the corresponding concept using photon-magnon coupling is presented.

Table of Contents

List of Figures

Chapter 1. Introduction

1.1. Moore's Law

In 1965, Dr. Gordon Moore observed a trend in integrated circuit manufacturing. The number of components minimizing the cost per component in an integrated circuit doubled every year [1]. Home computers, mobile phones, and various technological innovations were foreseeable from these predicted exponential performance increase and relative cost decrease. 10 years later, in 1975, Dr. Moore updated his projection to the doubling of transistors every two years, for what is now known as the Moore's Law [2].

Moore's Law drove the Information Technology industry. Coordinated efforts of worldwide manufacturers and suppliers of the semiconductor industry led to the sustained scaling down of circuit elements, turning Moore's Law into a self-fulfilling prophecy [3].

While scaling down transistors usually improved clock speed and power consumption, heat dissipation, which depends on the two variables, became a significant issue below 90nm [4]. To remain within power levels that can be dissipated, and since the supply voltage was not going any lower, the clock speed increase was hindered. Therefore, despite the continued increased transistor

1

density, single processor performance grew slower since the 2000s after years of exponential growth [5].

This expectation gap between Moore's Law and computing efficiency opens the way for dramatic innovations in computing [5]. In 2016, the International Technology Roadmap for Semi-Conductor changed its Moore's Law-centered strategy for the More than Moore approach. The focus for chips development includes diversification in architectures and devices [6].

1.2. Artificial Intelligence

The question of Artificial Intelligence (AI) can be found since the early days of computing in Alan Turing's papers [7]. AI, which aims to implement human cognitive functions such as learning and problem solving in machines or computers, has considerably grown in recent years due to the development of new hardware such as Graphical Processing Unit (GPU) and the availability of large datasets. AI shows its usefulness in various applications and sectors such as image and speech recognition, materials science, medicine, or finance.

AI relies on Artificial Neural Networks (ANN) such as Deep Neural Networks (DNN) and Recurrent Neural Networks (RNN) and other Machine Learning (ML) concepts to compute [8]. Those

concepts usually require a considerable amount of data with numerous matrix multiplication to work successfully. Consequently, Moore's Law expectation gap and the von Neumann bottlenecks (the physical separation of memory and processors) hinder the further development of AI. The research for new AI hardware and architectures is at the core of neuromorphic computing device research.

1.3. Neuromorphic Computing

The physicist Carver Mead introduced the term Neuromorphic Computing (NC) in 1989 [9]. Initially, NC described the use of silicon-based electronic systems to reproduce brain-like computation, mainly for neuroscience and simulation purposes. This definition evolved over the years to include the research for new AI hardware, architectures, and algorithms by intrinsically mimicking biological brain structures instead of simply running brain-inspired ANN algorithms on CPUs and GPUs [10].

The brain can be seen as a highly interconnected and energy-efficient computer operating at a different time and spatial scales [11]. Around 80% of the brain's volume is made by the cerebral cortex, the walnut-like outer shell responsible for a

considerable part of information processing. The cerebral cortex is divided between the left and right hemispheres into four lobes (frontal, parietal, occipital, and temporal). In each lobe, several areas assuming one or a few specific functions can be further distinguished.

Zooming in further in the spatial scale allows us to see neurons and synapses. Electrical potential spikes generated by neurons are used in the brain to encode information, communicate and compute. A neuron is composed of dendrites which are filaments used to receive inputs from other neurons, a cell body where inputs can be stored through the cellular membrane voltage and capacitance, and an axon used for sending outputs to other neurons. The Leaky, Integrate, and Fire model [12]−[15] can describe a neuron's basic behavior. Inputs from other neurons coming from dendrites are added up in the cell (integrate). This potential leaks over time towards the resting potential level (leaky). If a potential threshold is exceeded, the neuron emits a spike (fire). Many more or less bio−plausible models exist [16].

The other main component in the brain is the synapse. A synapse is a tiny gap making the interface between a dendrite and a neuron's body. Electrical signals transported by ions flowing through the synapse can be reinforced or inhibited by the synapse

capacitance modulation, thus realizing in-memory computing. This capacitance or "weight" storage and adaptation is at the basis of memory and learning. How the weight evolves describes a learning rule, whereas the ability to evolve is called synaptic plasticity. The Long- or Short-Term Potentiation and Depression (LTP/LTD, STP/STD) [17] plasticity are the synapse abilities to change their weights for milliseconds to hours and weeks. The Spike Timing Dependent Plasticity (STDP) [18] and the Spike Rate Dependent Plasticity (SRDP) [19] learning rules increase or decrease the synaptic weights according to the time difference between post and pre-synaptic spikes or to the pre-synaptic firing rate.

Therefore, the brain, which contains approximately 10^{15} synapses and 10^{11} neurons perform simultaneous computations directly at the memory location. As a result, our brains can simultaneously and accurately complete multiple tasks such as language, visual, and audible information processing, to name only a few, using only 20 Watts. To reproduce this energy efficiency and performance on a chip, neuromorphic device research aims to create neurons and synapses properties in new devices with highly interconnected architectures.

1.4. Emerging Neuromorphic Devices

Emerging neuromorphic devices can be classified depending on the main physical mechanisms at play [16]. For instance, emerging devices can rely on anion or cation migration [20], phase change [21], ferroelectricity [22], magnetism, and spintronics [23]. Up-and-coming synaptic devices are memristors [24] organized in crossbar arrays [25], while spintronics Spin-Torque Nano-Oscillators (STNO) show promising applications as nano-neurons [26]-[30].

This thesis explores a new field at the interplay between spintronics, magnetism, quantum optics, and microwave engineering, namely Photon-Magnon Coupling [31],[32], for realizing a neuromorphic neuron.

1.5. Photon-Magnon Coupling

Strong light-matter interactions can create new quasi-particles, called polaritons, which are hybrids of light and matter states [33]. Strong light-matter interactions have been typically observed in crystals between photons (the quanta of electromagnetic waves) and phonons (the quanta of lattice vibration). In such a system, the two independent harmonic oscillators couple through

6

light-matter interactions leading to 2 polaritons modes [34]. The frequency dispersion of the two modes shows independent phonon- and photon-like behaviors far from the zero-detuning point ($\Delta_\omega = \omega_{phonon} - \omega_{photon}$), whereas modes anti-crossing is observed near $\Delta_\omega = 0$.

The emerging field of Cavity Quantum Electrodynamics (CQED) experimentally observed anti-crossing between a photon cavity mode and a single 2-level atom in 1992 [35] and 1996 [36]. Over the years, anti-crossing, which is often seen as the signature of strongly-coupled quantum particles, has been observed with multiple systems [37] such as excitons in semiconductors [38], qubits in superconductors [39], and Rydberg atoms [40].

Anti-crossing between microwave photons and magnons was theoretically predicted in 2010 [41]. In 2013, strong photon-magnon coupling was experimentally demonstrated between a YIG sample and a superconducting coplanar microwave resonator at cryogenic temperatures [42]. In 2014, different coupling regimes (strong, weak, Magnetically Induced Transparency, Purcell Effect) were shown at room temperature between a YIG sphere and a 3-dimensional cavity [43]. The quasi-particle resulting from strong photon-magnon

interactions in a cavity is called Cavity Magnon-Polariton (CMP). Classical, electrodynamical, and quantum theories of the transmission line shape have been developed over the years [44],[45].

In 2014, strong photon-magnon coupling was shown between a single crystal YIG sphere and a Split-Ring Resonator (SRR), a 2-dimensional photon cavity [46],[47]. While previous studies focused on superconducting cavities at cryogenic temperatures or 3-dimensional cavities at room temperature, this study opened the path for 2-dimensional systems at room temperature. In particular, strong photon-magnon coupling was observed between an Inverted Split-Ring Resonator (ISRR) and an YIG film in 2017 [48], which is a similar system to the one used in this thesis.

Besides fundamental physical interests, achieving strong coupling between quantum systems enable technological progress [49], [50]. For instance, the field of Quantum Information Processing and Communication (QIPC) may use photons for transmitting information, superconducting systems for processing, and spin ensembles for information storage [37]. Such envisioned hybrid system needs to exchange data between its various components. Transducing information requires preserving coherence (phase

preservation of excitations). Since the transduction rate is proportional to the coupling strength and decoherence is proportional to the damping rates, the coupling strength must be higher than the damping rates: this is the strong coupling regime. Other applications include quantum repeaters [51] and quantum memories [52].

1.6. Thesis Outline

This thesis aims to create a neuromorphic neuron device from photon−magnon coupling in a hybrid magnonics system [53]. The hybrid system consists of an ISRR loaded with an YIG film. In this planar system, strong photon−magnon coupling results in anti−crossing [45], [48]. The CMPs are used as neurons: in the coupling range, the properties of the resulting CMPs, such as the S21 parameter magnitude, frequency, and phase, can be used as neuron functions. Those functions are used separately to perform a waveform classification task (classification between sine and square waveforms) in the reservoir computing framework, following what was previously done for single STNOs [28].

Additionally, the concept of vowel recognition based on the photon−magnon coupling is presented in the last part. Following [27], frequency recognition can be realized by encoding information in the

synchronization between an oscillator frequency and the frequency of an additional driving force. Using two additional frequencies, the resulting synchronization map in an array of oscillators leads to multiple synchronization states, which are used to encode, and hence recognize, input vowels. The numerous coupling ranges in photon－magnon coupling between photon oscillators and the magnon oscillator in an array of SRR photon resonators reproduces the idea of synchronization range and should allow performing the recognition. Since only the concept has been laid down by the time the thesis was written, the thesis is mainly focused on waveform recognition, and vowel recognition is presented in the last chapter.

Chapter one provided a historical overview of the IT industry leading to AI and the need for new neuromorphic devices. An overview of photon－magnon coupling summing up its main features and applications was given, ending up with a new possible application in the field of the neuromorphic device.

Chapter 2 lays down further the theoretical knowledge required in this thesis. The computing paradigm, reservoir computing, is explained in detail. Following RC, the classification task to perform is presented. Finally, classical and electrodynamical theories of PM coupling are discussed.

Chapter 3 explains the precise experimental setup and parameters, and procedure. The hybrid system and the neuron functions are shown.

Chapter 4 presents the results. Experimental and simulation recognition success rates are given for different configurations (ISRR alone, YIG alone, 2 YIG positions, two magnetic field angles, degenerate waveform sequences).

Chapter 5 presents the concept of vowel recognition using photon-magnon coupling.

Chapter 6 concludes the thesis, discusses the results, and suggests further work.

Chapter 2. Literature Review

Chapter 2 offers a review of reservoir computing and photon-magnon coupling theory. The recognition task is also explained.

2.1. Reservoir Computing

Reservoir computing (RC) is a neuromorphic computing framework based on Recurrent Neural Networks (RNN) [54]. In an RNN, feedback loops and neurons dynamical behavior enable the processing of temporal data. RC appeared after the development of Echo State Networks and Liquid State Machines as a unified framework for RNN-based networks [55]. This subchapter starts by explaining the general working principle of RC and the specific RC framework used in this thesis [56].

2.1.1. Classical Scheme of Reservoir Computing

The basic functionality of RC is data classification. Inputs to classify are sent to a network made of non-linear and randomly interconnected units called neurons. This Neural Network (NN), called a reservoir, also possesses randomly defined recurrent connections. Such a network is thus called a Recurrent Neural Network (RNN).

Connection values (thereafter called weights) between the input layer and the reservoir are randomly fixed. On the other hand, reservoir−to−output−layer weights change. This evolution follows a supervised learning rule while all the other weights remain identical. Weights of recurrent connections can either remain fixed or evolve via an unsupervised algorithm (figure 1.a).

The neuron activation function is the relationship between the neuron's output and its inputs. In an artificial (algorithmic) implementation of RC, the neuron function is often the hyperbolic tangent function. In that case, a general equation giving the neuron's output is:

$$x(t + 1) = f(W^{in} * u(t + 1) + W * x(t) + W^{fb} * \hat{y}(t)) \quad (2.1.1)$$

With $x(t)$ the vector describing the reservoir state (N−dimensional vector with N the number of neurons), u the input vector, $\hat{y}(t)$ the output state vector, f the neuronal activation function (tanh), W^{in} the input layer to the reservoir weight matrix, W the reservoir internal weight matrix and W^{fb} an optional matrix for output−layer−to−reservoir weights.

A general output layer activation function is:

$$\hat{y}(t) = f^{out}(W^{out} * [1, x(t), u(t), \hat{y}(t-1)]) \qquad (2.1.2)$$

f^{out} is usually the identity function, W^{out} is the weight matrix whose values are found by learning via linear regression, $\hat{y}(t-1)$ is the previous output vector, $u(t)$ is the input vector, $x(t)$ is the vector containing each neuron output, and $[., \cdots,.]$ is the vertical concatenation. The unitary vector 1 corresponds to adding a bias in the linear regression. In terms of RC, the bias corresponds to a neuron always equal to 1.

In this work, the output layer activation function is simply:

$$\hat{y}(t) = W^{res-out} * [1, x(t)] \qquad (2.1.3)$$

With $W^{res-out}$ the reservoir−to−output weight matrix.

When an input signal is applied, neurons responses are measured and combined linearly at the output layer. The network's output can be equivalently rewritten as:

$$\hat{y}(t) = \sum_{i=1}^{N} w_i^{res-out} * x_i(t) \qquad (2.1.4)$$

Where $\hat{y}(t)$ is the network output, $x_i(t)$ is the ith neuron response, $w_i^{res-out}$ is the weight between the ith neuron and the output layer.

A learning algorithm adjusts the weights. The goal is to find the weights so that the nth input type, among p different input types to be classified, gives for the nth output $\widehat{y_n}$:

$$\begin{cases} \widehat{y_n}(t) = 1 \\ \widehat{y_{m \neq n}}(t) = 0 \end{cases} \qquad (2.1.5)$$

For all $n, m \in [1,..,p]$.

Separating different types of input using linear combinations of non-linear functions is called a linear classifier.

2.1.2. Training and Testing a Reservoir Computer

RC is a paradigm change in the way recurrent networks are trained (figure 1.a). Usually, all weights are changed: the weights from the input layer to the reservoir, the weights inside the reservoir, and the weights from the reservoir to the output layer. RC only changes the weights from the reservoir to the output layer. This considerable reduction of trained parameters makes reservoirs easier to train than other types of RNN.

To find the matrix elements $w_i{}^{res-out}$ of the reservoir-to-output weight matrix $W^{res-out}$, each neuron output is measured for a

whole input sequence. For N neurons, one bias neuron $x_0 = 1$ and M inputs, the reservoir state is a $((N+1)*M)$ dimensional matrix:

$$R \equiv \begin{pmatrix} x_0 & \cdots & x_0 \\ \vdots & \ddots & \vdots \\ x_N(1) & \cdots & x_N(M) \end{pmatrix} \qquad (2.1.6)$$

Next, we define the weight matrix $W^{res-out}$. In general, $W^{res-out}$ is a $(p*(N+1))$ dimensional matrix, with p the number of input types or, equivalently, the number of linear classifiers to train. In this thesis, since inputs are classified between 2 categories, one linear classifier is enough. Therefore, we obtain:

$$W^{res-out} \equiv (w_0{}^{res-out} \quad \cdots \quad w_N{}^{res-out}) \qquad (2.1.7)$$

The following step is to define the targeted output matrix Y. Y is a $(p*M)$ dimensional matrix. For two types of inputs, the matrix elements y of Y equal 1 when one category is applied to the system and 0 for the second. As the learning dataset is known, this matrix is also known. With M number of inputs and one linear classifier to train, we have:

$$Y \equiv (y(1) \quad \cdots \quad y(M)) \qquad (2.1.8)$$

Similarly, we define the $(p*M)$ output matrix, which contains the linear combinations $\widehat{Y}$, as:

$$\hat{Y} \equiv (\hat{y}(1) \quad \cdots \quad \hat{y}(M)) \qquad (2.1.9)$$

The training goal is to determine the weights $W^{res-out}$ to fit $\hat{Y}$ with Y. This is done by minimizing the mean square error:

$$MSE = \|\hat{Y} - Y\|^2 = \|W^{res-out} * R - Y\|^2 \qquad (2.1.10)$$

This is done by choosing:

$$W^{res-out} = (Y * R^{\dagger})^T \qquad (2.1.11)$$

Where † denotes the Moore−Penrose pseudo−inverse.

After learning, an unseen dataset is applied to the system. This is the testing phase. Each neuron output is measured, and the trained weights $W^{res-out}$ are used to calculate the linear combinations according to:

$$\hat{Y} = W^{res-out} * R \qquad (2.1.12)$$

The trial is a success if:

$$\begin{cases} \hat{y}(i) > 0.5 \; and \; y(i) = 1 \\ \hat{y}(i) < 0.5 \; and \; y(i) = 0 \end{cases} , \; for \; i \in [1,..,M]. \qquad (2.1.13)$$

And is a failure otherwise. The number of successes to the number of trials ratio gives the success rate. Success rates under various experimental conditions are the main results reported in this thesis.

2.1.3. Reservoir Requirements

Neurons in the reservoir must meet several requirements for the classification to work. Three main requirements are discussed here.

The first and most basic requirement is neuronal non-linearity since in RC, classification requires signals to be non-linearly projected into the reservoir space by the neuron function.

The second requirement is the reservoir size. Separating inputs with linear classifiers requires a highly dimensional reservoir. Hundreds or thousands of neurons can be necessary to achieve good performances.

The final requirement is memory. Depending on the task, neurons may or may not require intrinsic short-term memory and feedback loops. A relevant example is a waveform sequence containing two types of waveforms: sines and squares. If both waveforms share a common value, the common value cannot be successfully classified without a memory. If the sequence is not degenerated, memory is not required.

2.1.4 Reservoir Computing with a Single Neuron

Reservoir size is a significant issue for hardware implementation of RC. In 2011, Appeltant et al. demonstrated RC with a single neuron [57]. By using unique data pre-processing, the entire reservoir can be emulated from a single hardware neuron. This is the method used in the thesis (figure 1.b).

The data pre-processing is illustrated in figure 1.c. Two types of signals can be sent as input: Time-continuous signals or time-discrete signals (u(t) and u(k), respectively). First, signals are sampled and held with a τ time periodicity. Then, each sampled value is multiplied by a mask M, a $(1 * N)$ matrix with N the number of neurons to emulate, where the ith value represents the input-to-i^{th} neuron weight [58]. In this work, following dr. Grolier's example [28], the mask is a random ± 1 binary sequence. The final step is time multiplexing. Each newly obtained value is held for a time Θ, with Θ=τ/N. The ith neuron is simply the single hardware neuron when the sampled input value times the ith mask value is applied to the system.

A delayed feedback loop with the same τ periodicity is added to the system if a short-term memory is desired. Since the

periodicities between the pre–processing and the loop are shared, the ith neuron will receive its previous output as an input as well.

The inter–neuron connection can be achieved by using the device's intrinsic relaxation time. Each pre–processed input value is held for a time Θ, with $\Theta = \tau/N$. If Θ is lower than the relaxation time, the $i^{th}+1$ neuron output will depend on the ith neuron output. To measure each virtual neuron output, the device response is red after each time step Θ. Because the network output linearly combines the N virtual neurons outputs, we obtain for any time t:

$$\hat{y}(t) = \sum_{i=1}^{N} w_i^{res-out} * x\left(t - \frac{\tau}{N}(N - i)\right) \qquad (2.1.14)$$

With one linear classifier to train, M sampled points to classify applied for a time τ, N neurons, and one additional bias neuron $x_0 = 1$, an equivalent matrix formulation is given by:

$$\hat{Y} = W^{res-out} * R' \qquad (2.1.15)$$

Where:
$$R' \equiv \begin{pmatrix} x_0 & & x_0 \\ x_1(\theta) & \cdots & x_1(M * \theta) \\ x_2(2\theta) & \ddots & x_2(M * 2\theta) \\ \vdots & & \vdots \\ x_N(\tau) & \cdots & x_N(M * \tau) \end{pmatrix}, \qquad (2.1.16)$$

$W^{res-out} \equiv (w_0^{res-out} \quad \cdots \quad w_N^{res-out})$ and $\hat{Y} \equiv (\hat{y}(\tau) \quad \cdots \quad \hat{y}(M * \tau))$.

Training and testing are following the classical scheme of RC.
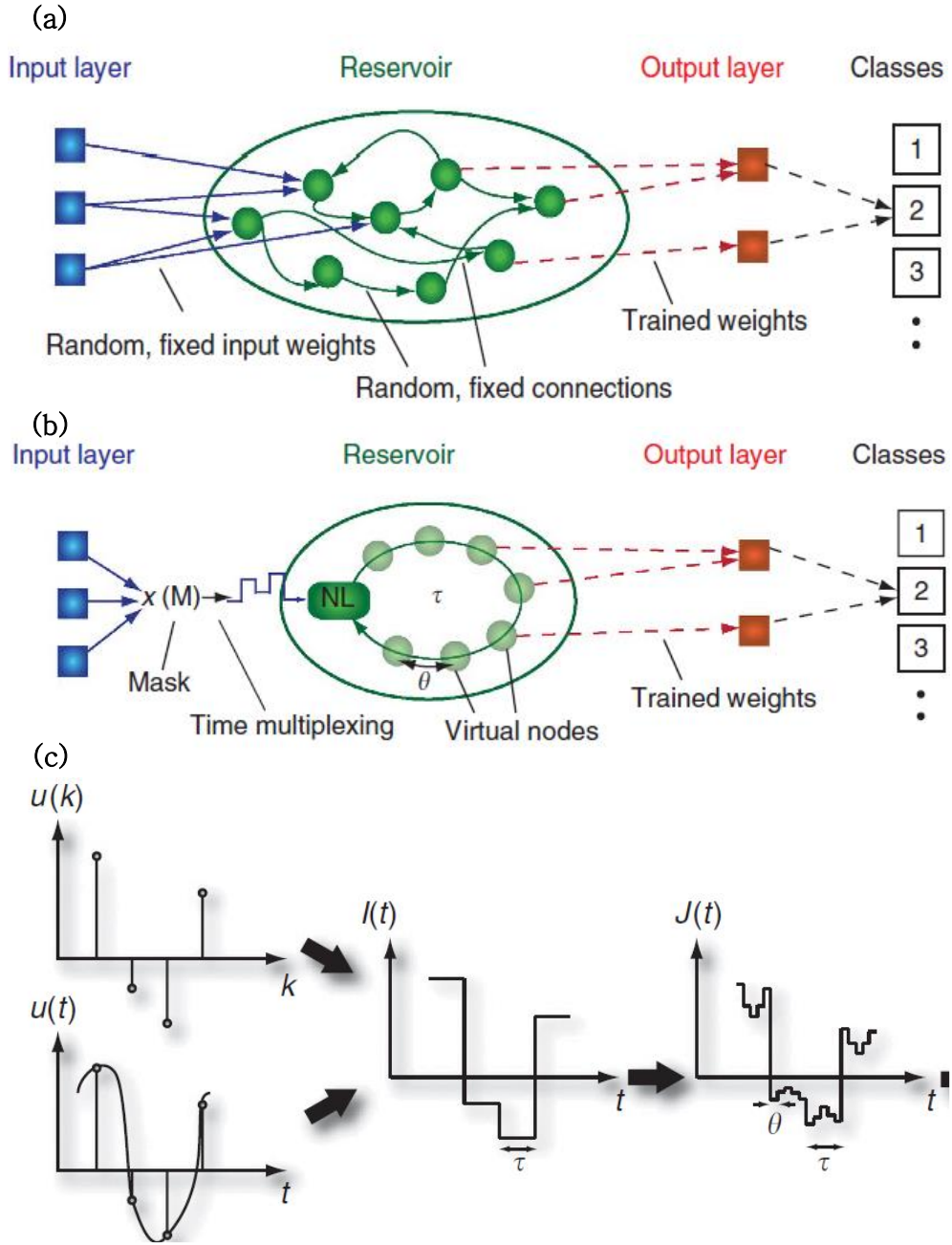
Figure 1. (a) RC scheme. (b) Single node RC scheme. (c) Data pre-processing [57].

2.1.3. Waveform recognition with single node RC

Hardware implementation of single node RC has been demonstrated with electrical systems [57],[59], mechanical systems [60]−[61], photonic systems [62]−[68], memristor array [69] and spintronics using STNOs [26]−[30], [70]. Waveform recognition of a degenerate [28] or non−degenerate [59] sequence is a typical benchmark task for RC with a single hardware node. Non−degenerate waveform recognition is the task performed in this thesis.

The first step towards recognition is the dataset creation. The dataset is made of a randomly defined sequence of sine and square waveforms with different amplitudes. Each waveform is made of a given number of sampled points (figure 3.a).

Following Appeltant et al. [57], each sampled point is multiplied by a mask defining the number of neurons (figure 3.b). According to an encoding scale, the resulting pre−processed data points are successively applied as inputs to the system for a given time Θ (figure 3.c).

In the training step, half of the data is used for finding the weights $W^{res-out}$ by minimizing the MSE. The other half is kept for testing the network output to find the success rates, using the trained

weights. The goal is to recognize the category of each sampled point by reconstructing the network outputs $\hat{Y}$ from the measured hardware response R'. The process is illustrated in Figures 2 and 3 for an STNO [28].

Besides the success rates, the Normalized MSE (NMSE) is also tracked:

$$NMSE = \frac{1}{n * var(y(n))} \sum_{i=1}^{n} (y(n) - \hat{y}(n))^2 \qquad (2.1.17)$$

Where $\hat{y}(n)$ is the network output and $y(n)$ is the target value.

Equivalently, the Nash-Sutcliffe Efficiency (NSE) can be tracked [71]:

$$NSE = 1 - NMSE \qquad (2.1.18)$$

The NMSE/NSE ranges in $[0,+\infty]/[-\infty,1]$. An NMSE/NSE equals 0/1 indicates a perfect prediction. On the other hand, an NMSE/NSE $\geq 1/$ ≤ 0 shows no added benefit from the network compared to a model equal to the target values' mean. By measuring the network output deviation from the target, both NMSE and NSE assess the prediction quality. Assessing the prediction quality allows to discriminate systems with equal success rates and to compare different neuron hardware.
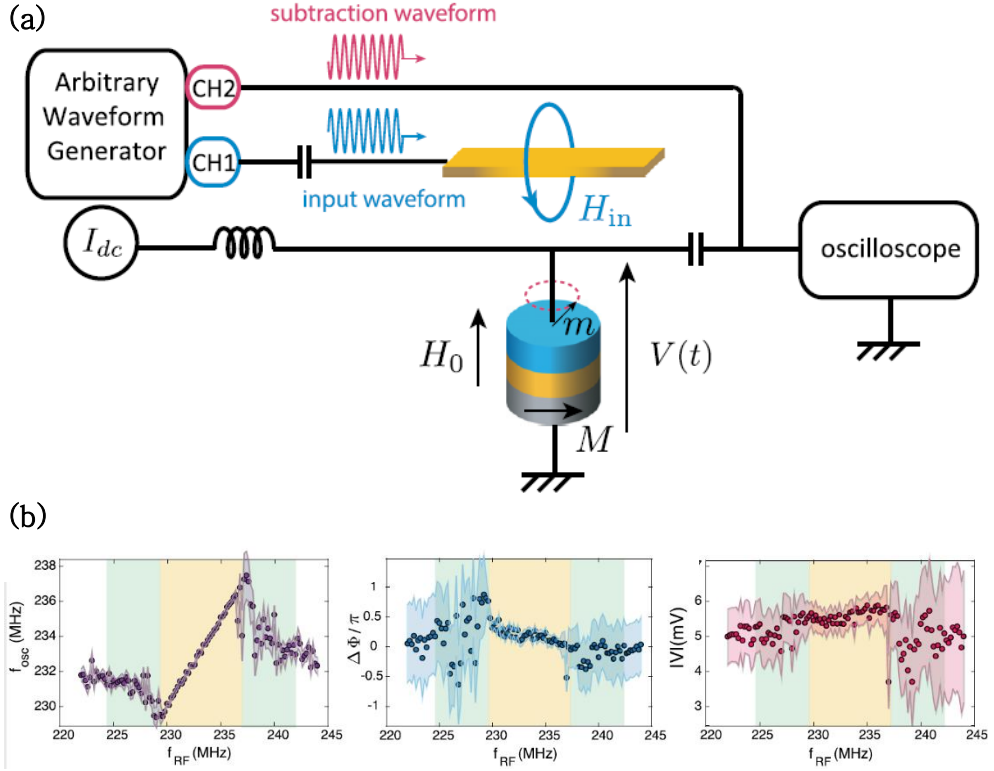
Figure 4. (a) Single node RC with an STNO for non−degenerate waveform recognition. The STNO interacts with $\boldsymbol{H_{in}}$ which encodes waveforms. (b) Neuron functions are the frequency (violet), phase (blue), and amplitude (red) of the STNO voltage as a function of the microwave current frequency. [28].
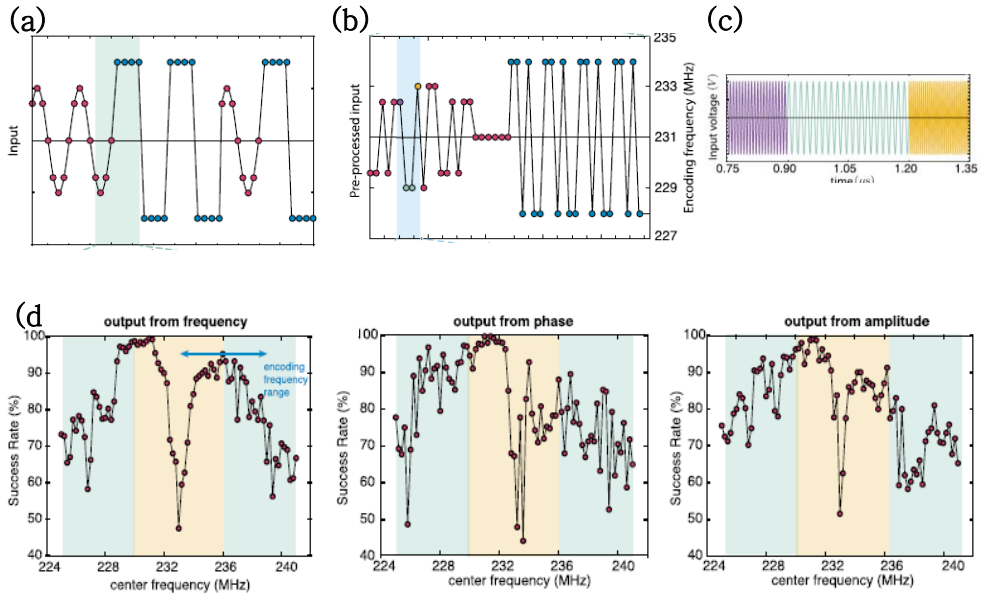
Figure 6. (a) Waveform sequence. (b) Mask multiplication. The black horizontal line represents the center frequency. (c) Conversion to a microwave current frequency. (d) Success rates from the frequency, phase and amplitude [28].

2.2. Photon-Magnon Coupling Theory

2.2.1. Spin Waves and Magnons

Interaction between electronic spins in atoms can lead to magnetic ordering [72]. In particular, exchange interaction between neighboring spins can lead to parallel (ferromagnetism) or antiparallel (antiferromagnetism) spin orientations.

Meanwhile, when a bias magnetic field is applied on a spin magnetic moment, a torque tends to align the magnetic moment on the field to decrease Zeeman potential energy. As a consequence, the magnetic moment undergoes a damped precession motion around the magnetic field according to the Landau-Lifshitz-Gilbert (LLG) equation [73]:

$$\frac{dm}{dt} = \gamma m \times H + \alpha m \times \frac{dm}{dt} \qquad (2.2.1)$$

When strong exchange interaction keeps all the spins parallelly aligned, the resulting uniform magnetization precession motion obeys the LLG equation, and the resonance frequency is given by:

$$\omega_r = \gamma\sqrt{H(H + \mu_0 M_S)} \qquad (2.2.2)$$

Where γ is the gyromagnetic ratio, H is the external magnetic field and $\mu_0 M_S$ is the saturation magnetization. This in-phase collective motion can be seen as a spin-wave of infinite wavelength called the

Kittel's mode. Alike electromagnetic fields and photons or crystal lattice vibrations and phonons, spin waves are quantized in magnons, a bosonic quasi-particle.

In thin-film magnetic samples, additional finite wavelength spin-wave modes can be excited [74]. Short wavelength modes are dominated by exchange interaction, while long-wavelength modes are dominated by magnetic dipolar interaction. Depending on the external magnetic field angle and the spin-wave propagation direction, different dipolar dominated spin waves, or magnetostatic waves, can be excited, as illustrated in figure 4.

While each spin-wave mode can couple with photons, the coupling strength is inversely proportional to the wavenumber [75], and the strongest coupling is usually achieved with Kittel's mode.
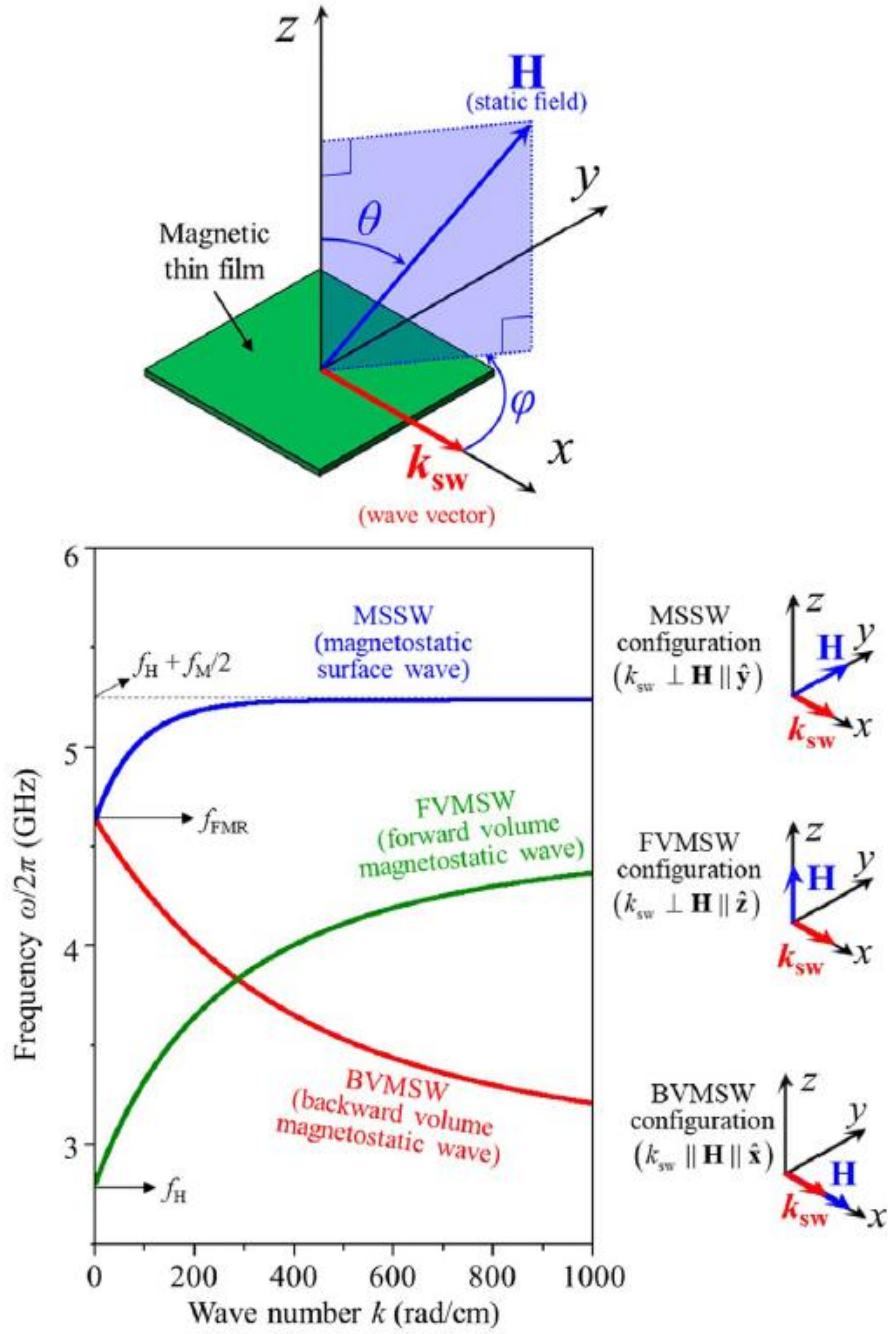
Figure 8. Spin-waves dispersion in a thin-film [31].

2.2.2. Classical Harmonic Oscillator Model

Photon–magnon coupling can be described by a classical harmonic oscillator model [44]. The cavity photon oscillator and the magnon oscillator resonance frequencies are respectively ω_c and ω_m. Photon and magnon losses are modeled by viscous forces of damping constants β and α. The oscillators are coupled by a spring of constant κ. In this first model, only the photon oscillator is driven by an external force $f(t) = fe^{-i\omega t}$ representing a microwave input of frequency ω.

Considering a unitary mass, Newton's Laws lead to the following equations of motion for the photon and magnon oscillators:

$$\ddot{x}_c + \omega_c^2 x_c + \beta\omega_c\dot{x}_c + \kappa\omega_c^2 x_m = fe^{-i\omega t}$$
$$\ddot{x}_m + \omega_m^2 x_m + \alpha\omega_m\dot{x}_m + \kappa\omega_c^2 x_c = 0 \qquad (2.2.3)$$

Assuming an oscillator motion of the form $x_{c,m}(t) = x_{c,m}e^{-i\omega t}$ ($\dot{x}_{c,m}(t) = -i\omega x_{c,m}(t)$; $\ddot{x}_{c,m}(t) = -\omega^2 x_{c,m}(t)$), we obtain in a matrix form:

$$\begin{pmatrix} \omega^2 - \omega_c^2 + i\beta\omega_c\omega & -\kappa\omega_c^2 \\ -\kappa\omega_c^2 & \omega^2 - \omega_m^2 + i\alpha\omega_m\omega \end{pmatrix} \begin{pmatrix} x_c \\ x_m \end{pmatrix} = \begin{pmatrix} -f \\ 0 \end{pmatrix} \quad (2.2.4)$$

The determinant of the 2∗2 matrix Λ is given by:

$$\det(\Lambda) = \left(\omega^2 - \omega_c^2 + i\beta\omega_c\omega\right)\left(\omega^2 - \omega_m^2 + i\alpha\omega_m\omega\right) - \kappa^2\omega_c^4 \quad (2.2.5)$$

Solving numerically for ω and plotting the real and imaginary parts gives the eigenmodes dispersion and their linewidth evolution (figure 5.a and 5.b for $\omega_c = 10.54 GHz$, $\alpha = 0.8 \times 10^{-4}, \beta = 3 \times 10^{-4}, \mu_0 H = -37.7 mT$).

Further analytical analysis can be done in the low damping case $(\alpha, \beta \ll 1)$ near the crossing point $(\omega \approx \omega_c \approx \omega_m)$. The 2∗2 matrix Λ becomes:

(2.2.6)

$$\Lambda = \begin{pmatrix} \omega^2 - \omega_c{}^2 & -\kappa \omega_c{}^2 \\ -\kappa \omega_c{}^2 & \omega^2 - \omega_m{}^2 \end{pmatrix} = \begin{pmatrix} 2\omega_c(\omega - \omega_c) & -\kappa \omega_c{}^2 \\ -\kappa \omega_c{}^2 & 2\omega_c(\omega - \omega_m) \end{pmatrix}$$

So, the determinant is:

$$\det(\Lambda) = 4\omega_c(\omega - \omega_c)(\omega - \omega_m) - \kappa^2 \omega_c{}^4 \qquad (2.2.7)$$

Approximating terms proportional to frequency sums by $2\omega_c$ while keeping terms proportional to differences is called the Rotating Wave Approximation (RWA).

The roots are given by:

$$\omega_\pm = \frac{\omega_c + \omega_m \pm \Omega_g}{2} \qquad (2.2.8)$$

Where we defined the generalized Rabi frequency as $\Omega_g = \sqrt{(\omega_c - \omega_m)^2 + \kappa^4 \omega_c{}^2}$.

Finding the eigenvectors $X_\pm = (u_\pm, v_\pm)$ is done by solving

30

the following matrix equations:

$$\begin{pmatrix} 2(\omega_\pm - \omega_c) & -\kappa\omega_c \\ -\kappa\omega_c & 2(\omega_\pm - \omega_m) \end{pmatrix} \begin{pmatrix} u_\pm \\ v_\pm \end{pmatrix} = \begin{pmatrix} 0 \\ 0 \end{pmatrix} \qquad (2.2.9)$$

Which can be simplified as:

$$\begin{pmatrix} \Delta \pm \Omega_g & -\kappa\omega_c \\ -\kappa\omega_c & -\Delta \pm \Omega_g \end{pmatrix} \begin{pmatrix} u_\pm \\ v_\pm \end{pmatrix} = \begin{pmatrix} 0 \\ 0 \end{pmatrix} \qquad (2.2.10)$$

Where $\Delta \equiv \omega_m - \omega_c$.

Solving the first line gives after normalization:

$$\begin{pmatrix} u_\pm \\ v_\pm \end{pmatrix} = \frac{1}{\sqrt{(\kappa\omega_c)^2 + (\Delta + \Omega_g)^2}} \begin{pmatrix} \pm\kappa\omega_c \\ \pm\Delta + \Omega_g \end{pmatrix} \qquad (2.2.11)$$

With $\sin(\theta) \equiv {}^{\kappa\omega_c}/_{\Omega_g}$ and $\cos(\theta) \equiv {}^{\Delta}/_{\Omega_g}$ we get:

$$\begin{pmatrix} u_\pm \\ v_\pm \end{pmatrix} = \frac{1}{\sqrt{2\Omega_g}} \begin{pmatrix} \pm\sqrt{\Omega_g \mp \Delta} \\ \sqrt{\Omega_g \pm \Delta} \end{pmatrix} \qquad (2.2.12)$$

Therefore, we finally get:

$$\begin{pmatrix} X_+ \\ X_- \end{pmatrix} = \begin{pmatrix} \eta_1 & \eta_2 \\ -\eta_2 & \eta_1 \end{pmatrix} \begin{pmatrix} \omega_c \\ \omega_m \end{pmatrix} \qquad (2.2.13)$$

With $\eta_1 = u_+$ and $\eta_2 = v_+$. The coefficients $\eta_1(\eta_2)$ and $\eta_2(\eta_1)$ give respectively the photon and magnon proportion of $X_+(X_-)$ (figure 5.c).
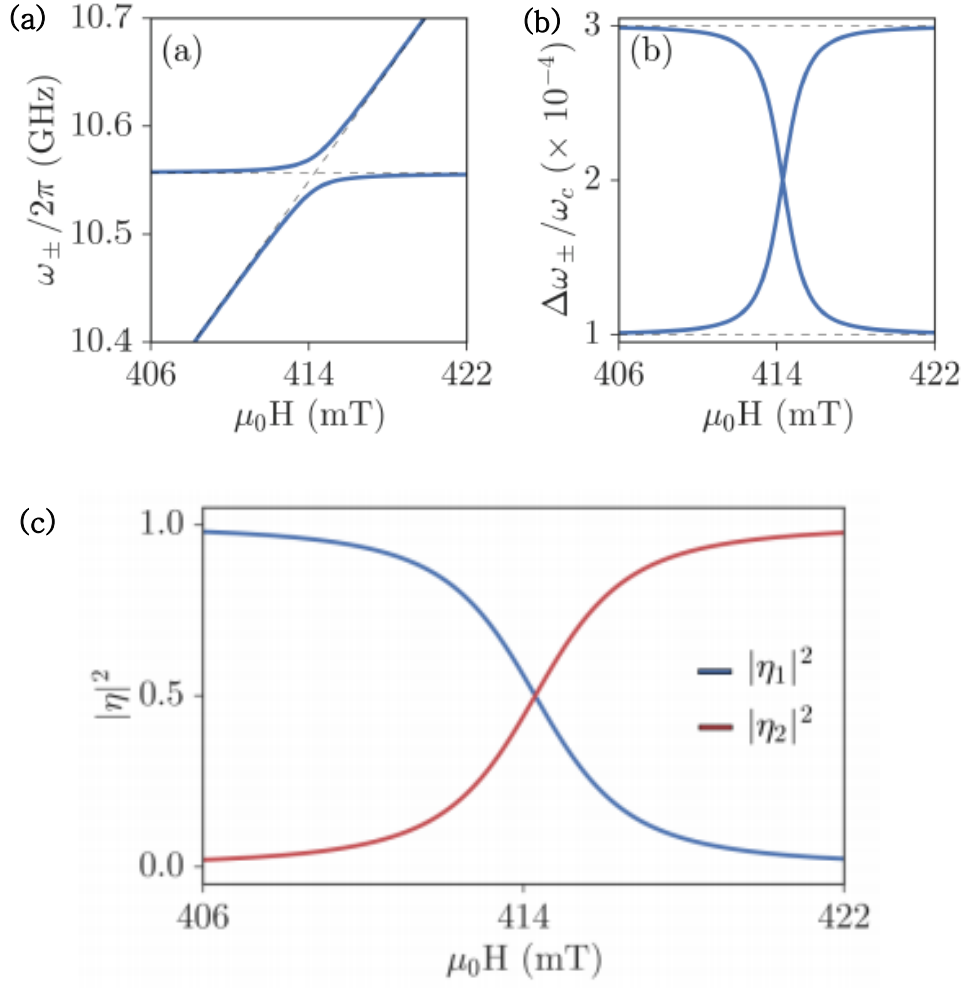
Figure 10. (a) Frequency dispersion and (b) linewidth dispersion of the CMP modes. (c) Evolution of η_1 and η_2 [44].

Finally, expressing the energy transmitted through the system requires adding an energy absorber coupled with the photon oscillator. Physically, such a third oscillator equation represents an output port connected to the cavity, whereas the driving force is applied to the cavity through an input port. Defining an impedance mismatch parameter Γ, the output to input energy ratio, the so−called S_{21} parameter is given by:

$$S_{21} = \Gamma \frac{\omega_c{}^4}{\omega^2} \frac{(\omega^2 - \omega_r{}^2 + i\alpha\omega\omega_c)}{\det(\Lambda)} \qquad (2.2.14)$$

2.2.3. Electrodynamical Model

PM coupling for the hybrid system used in this thesis was described by Bhoi et al. [45]. In this electrodynamical model, the driving force $f(t)$ excites both cavity photons and magnons. $f(t)$ represents an RF current flowing through a microstrip line. The photon cavity is a planar Inverted Split Ring Pattern (ISRR) etched on the ground plane of the microstrip line [76],[77]. $f(t)$ drives the photon oscillator by inducing an RF current in the planar cavity while it can directly excite magnons through Ampere's circuit law. Coupling comes from electromagnetic interactions. When excited, the photon cavity creates an RF magnetic field that interacts with magnons from a ferromagnetic film. On the other hand, magnons from the ferrimagnetic film induce additional currents in the planar cavity according to Faraday's Law.

The voltage created in the cavity by the AC current $\mathbf{j}$ from the microstrip line is given by $\mathbf{V} = \mathbf{Z_{ISRR}j}$. With $\mathbf{L}$ the ISRR inductance, $\mathbf{C}$ its capacitance, $\boldsymbol{\omega_{ISRR}} = \mathbf{1}/\sqrt{\boldsymbol{LC}}$ its resonance frequency, the ISRR impedance $\boldsymbol{Z_{ISRR}}$ is given by:

$$Z_{ISRR} = -\frac{iL}{\omega}(\omega^2 - \omega_{ISRR}{}^2 + 2i\beta\omega_{ISRR}\omega) \qquad (2.2.15)$$

Following Faraday's Law, magnons induce an additional voltage in the ISRR proportional to the oscillating magnetization vector $\boldsymbol{m}^+$. The voltage is given by:

$$V_{ISRR \leftarrow YIG} = -K_F L \omega m^+ \qquad (2.2.16)$$

Where $\boldsymbol{K_F}$ is a coupling constant from Faraday's Law. Adding the induced current to $\mathbf{j}$, the total current $\boldsymbol{J}^+$ in the ISRR is given by:

$$J^+ = \mathbf{J} e^{-i(\omega t + \varphi)} \qquad (2.2.17)$$

Where $\boldsymbol{\varphi}$ is the phase difference between the ISRR current and the microstrip line current. With $\boldsymbol{V_{ISRR \leftarrow YIG}} = \boldsymbol{Z_{ISRR} J^+}$ and $\mathbf{V} = \boldsymbol{Z_{ISRR} J^+}$, we can write the equation for the cavity photon mode:

$$iK_F \omega^2 m^+ + \left(\omega^2 - \omega_{ISRR}{}^2 + 2i\beta\omega_{ISRR}\omega\right)J^+ = 0 \qquad (2.2.18)$$

The magnon equation is obtained from the linearized LLG equation [80]. By considering both the oscillating magnetic field coming from the microstrip line $\boldsymbol{h_{line}} = \mathbf{h} e^{-i\omega t}$ and the ISRR magnetic field $\boldsymbol{h_{ISRR}} = \frac{|h_{ISRR}|}{|h_{line}|} e^{-i\varphi} = \delta e^{-i\varphi} \boldsymbol{h_{line}}$ as exciting oscillating fields, they obtained after using Ampere's Law :

$$(\omega - \omega_r + i\alpha\omega)m^+ - i\omega_m K_A\left(1 + \delta e^{i\varphi}\right)J^+ = 0 \qquad (2.2.19)$$

Where $\boldsymbol{K_A}$ is a coupling constant coming from Ampere's Law and

$\omega_m = \gamma \mu_0 M_S$. The 2*2 matrix $\boldsymbol{\Lambda}$ becomes:

$$\boldsymbol{\Lambda} = \begin{pmatrix} (\omega^2 - \omega_{ISRR}{}^2 + 2i\beta\omega_{ISRR}\omega) & iK_F\omega^2 \\ -i\omega_m K_A(1 + \delta e^{i\varphi}) & (\omega - \omega_r + i\alpha\omega) \end{pmatrix} \quad (2.2.20)$$

Solving the real part of $\det(\boldsymbol{\Lambda})$ gives the following dispersion relation:

$$\omega_\pm = \frac{1}{2}[(\omega_r + \omega_{ISRR}) \pm \sqrt{(\omega_r - \omega_{ISRR})^2 + (4\pi\Delta)^2}] \quad (2.2.21)$$

With $\Delta = \frac{1}{4\pi}\sqrt{2K^2\omega_m\omega_{ISRR}(1 + \delta cos\varphi)^2}$ and $K^2 \cong K_A K_F$

And the $\boldsymbol{S_{21}}$ parameter is:

$$\boldsymbol{S_{21}} = \Gamma\frac{J^+}{j} = \Gamma\frac{\omega^2(\omega - \omega_r + i\alpha\omega)}{\det(\Lambda)} \quad (2.2.22)$$

From this equation, the $\boldsymbol{S_{21}}$ parameter and phase of the cavity, magnon mode, and coupled systems can be plotted in the $\boldsymbol{\omega - H}$ plane, or equivalently, in the $\boldsymbol{\omega - I}$ plane, where I is the current flowing through the electromagnet generating $\boldsymbol{H}$ (figure 6). While such plots are usually drawn in the $\boldsymbol{\omega - H}$ plane, the $\boldsymbol{\omega - I}$ plane is more convenient for this research work. Figure 6 clearly shows the mode splitting around the anti-crossing point (current value where $\boldsymbol{\omega_r = \omega_{ISRR}}$). The plotting was done with $\boldsymbol{\omega_c = 4.0 GHz, \mu_0 H = 0.172T, \alpha = 3.2 \times 10^{-4}, \beta = 2 \times 10^{-2}, \Gamma = 0.04, K = 0.045, \delta = 0.5, \varphi = 0}$.
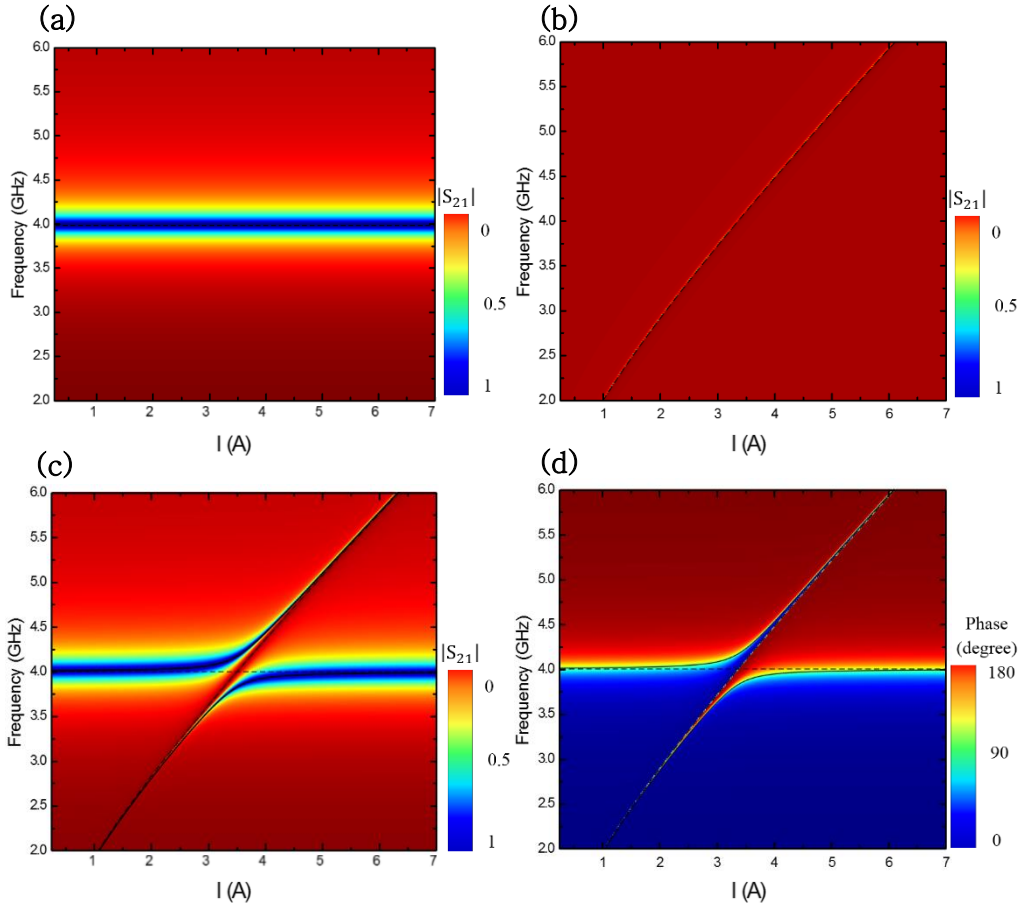
Figure 12. S_{21} parameter of (a) the ISRR alone, (b) magnons alone, and (c) coupled system. (d) Phase of the coupled system. Solid black lines are the fitted upper and lower branch of the frequency dispersion. Horizontal and vertical dotted black lines are respectively the cavity and magnon frequency.

Chapter 3. Experimental Method

3.1. Observing Photon—Magnon Coupling

Observing strong photon—magnon coupling requires a high—quality cavity and low damping magnons. Hybrid systems used for photon—magnon coupling usually combine a 2— or 3—dimensional photon cavity with an Yttrium Iron Garnet ferrimagnetic sphere or thin film. In this thesis, a 2—dimensional cavity along with a YIG thin film were used. Meanwhile, S_{21} parameters are measured from Vector Network Analyzer (VNA) calibrated two ports measurements. The measurement technique and the two subsystems are presented in this sub—chapter.

3.1.1. Microwave Measurement

The S_{21} parameter is the energy transmitted through the system. According to equations (2.2.14) and (2.2.22), at the photon and magnon frequencies for an uncoupled system or at the CMP resonance frequency for a coupled one, the system strongly absorbs microwave energy, and dips in the transmission spectra are observed. In general, S—parameters for a 2—port system can be measured with a VNA [78]. The S—parameters are given by $\boldsymbol{S_{ij}} = \frac{V_i^-}{V_j^+}$, where $\boldsymbol{V_i}^-$ is

38

the microwave voltage reflected from port **i** and $V_j{}^+$ is the voltage sent to port **j**. Therefore, during an S_{21} parameter measurement, the VNA measures the ratio of microwave voltage received at port 2 to the microwave voltage sent from port one for different angular frequencies $\boldsymbol{\omega}$.

The VNA used in the experiments is an Agilent Technologies E8362C PNA Network Analyzer. Both S_{21} parameter and phase are measured in a dedicated channel. Measurements were performed from 2GHz to 6GHz with 6401 points per trace. The sweeping rate, or IF Bandwidth, was set to 10kHz to have a fast sweeping rate. Even though both channels were calibrated, post−measurement data calibration was required for phase measurements to subtract a linear phase shift induced by the hybrid system. The first measured point was set to 0 degree, and the linear phase shift, measured between 2GHz and 2.5 GHz (far from resonance), was removed from the trace. The VNA was entirely controlled by a computer using LabVIEW and RS232.

3.1.2. Photon System: Inverted Split-Ring Resonator

Split-Ring Resonators (SRR) are an essential building block for metamaterials [76],[77]. SRRs can be used to engineer magnetic permeability and negative refractive index [79]. An SRR is a split ring or square made of a conductive material deposited on a dielectric substrate in its simplest form. This structure shows a geometry dependant resonant frequency $\boldsymbol{\omega_c} = \frac{\mathbf{1}}{\sqrt{LC}}$, with L the SRR inductance and C the SRR capacitance given by:

$$\mathbf{C} = \boldsymbol{\varepsilon_0}\boldsymbol{\varepsilon_c}\frac{rt}{g} \ , \mathbf{L} = \boldsymbol{\mu_o}\frac{l^2}{t} \qquad (3.1.1$$

With $\boldsymbol{r}$ the ring width, $\boldsymbol{g}$ the gap length, $\boldsymbol{t}$ the metal thickness, and $\boldsymbol{l}$ the ring length.

SRRs can be excited by a microstrip line. Current flowing in the microstrip line induces a current in the ring and a magnetic field perpendicular to the ring plane. The system behaves as an LC circuit: the gap behaves like a capacitor while the ring behaves like a coil. In an Inverted Split Ring Resonator (ISRR), the SRR is patterned in the substrate's ground plane just below the microstrip line, and the role of the gap and the ring are switched (figure 7.a). The linear phase shift stated in part 3.1.1 comes from the microstrip line and is a standard and to be expected strip line behavior (figure 8.c).

Using CST studio, an electromagnetic simulation software, the dimensions of a 4.3GHz square−shaped ISRR were found. This ISRR is situated below a 50 Ohms microstrip line whose dimensions were found by the App−CAD calculator. The resonator was patterned using photolithography and conventional printed circuit board techniques from a CER−10RF substrate. Two SMA connectors were soldered at the ends of the microstrip line to send microwave currents (Figures 7.b and 7.c).

The fabricated ISRR has a 4.376GHz resonant frequency. The damping is $\beta = \Delta_{HWHM}/\omega_{ISRR} = 9.0e7/4.375e9 \approx 0.0206$, where Δ_{HWHM} is the half $\omega_C = 1/\sqrt{LC}$ width at half maximum. Δ_{HWHM} was estimated by fitting the S_{21} measurement of the ISRR alone and without magnetic field with a Lorentzian function while ω_{ISRR} was obtained from the measured S_{21} parameter. S_{21} magnitude and phase measurements using the VNA were done for different magnetic field values and are shown in figure 8. The x−axis I(A) represents the current sent to the electromagnet. The ISRR properties remain unchanged as the magnetic field is swept.
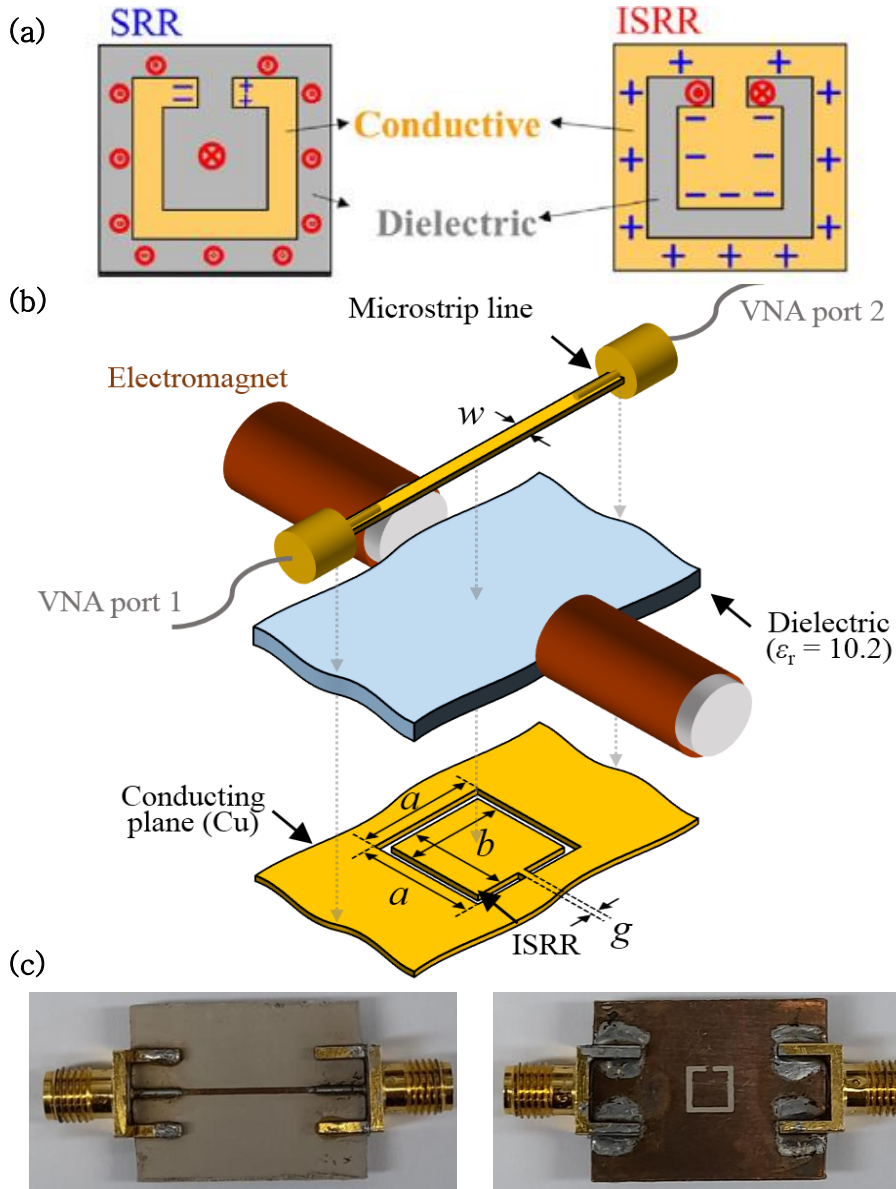
Figure 14. (a) SRR and ISRR schematic with electric fields (blue), and magnetic fields (red) [31]. (b) Schematic of the measurement setup. (c) Fabricated ISRR, w=0.6mm, a=4.4mm, b=3.4mm, g=0.5mm, the copper thickness is 35um, and the dielectric thickness is 0.64mm.
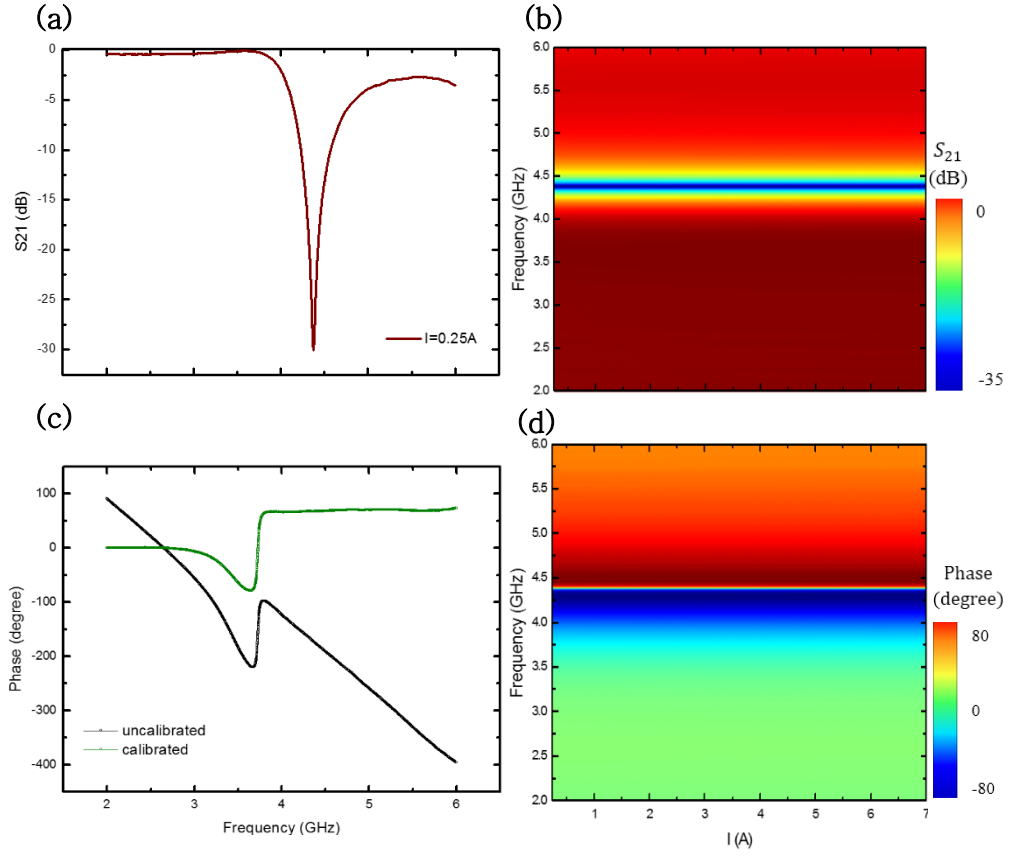
Figure 16. (a) Measured ISRR S_{21} parameter. (b) Measured ISRR S_{21} parameter in the $\omega - I$ plane. (c) Uncalibrated and calibrated ISRR phase. (d) Calibrated ISRR phase in the $\omega - I$ plane.

3.1.3. Magnon System: Yttrium Iron Garnet

Our magnon source is a commercial 3.7x3.7x25μm epitaxial YIG film ($Y_3Fe_5O_{12}$). YIG is the commonly used material in photon−magnon coupling studies owing to its high spin density ($\approx 4.0 * 10^{27}m^{-3}$) and very low damping ($\approx 3 * 10^{-5}\ to\ 10^{-3}$) [80]. Previous S21 parameter measurements of our YIG alone determined the magnon damping at $\boldsymbol{\alpha = 3.2 \times 10^{-4}}$ [45]. The magnon frequency follows Kittel's mode (figure 9.b).
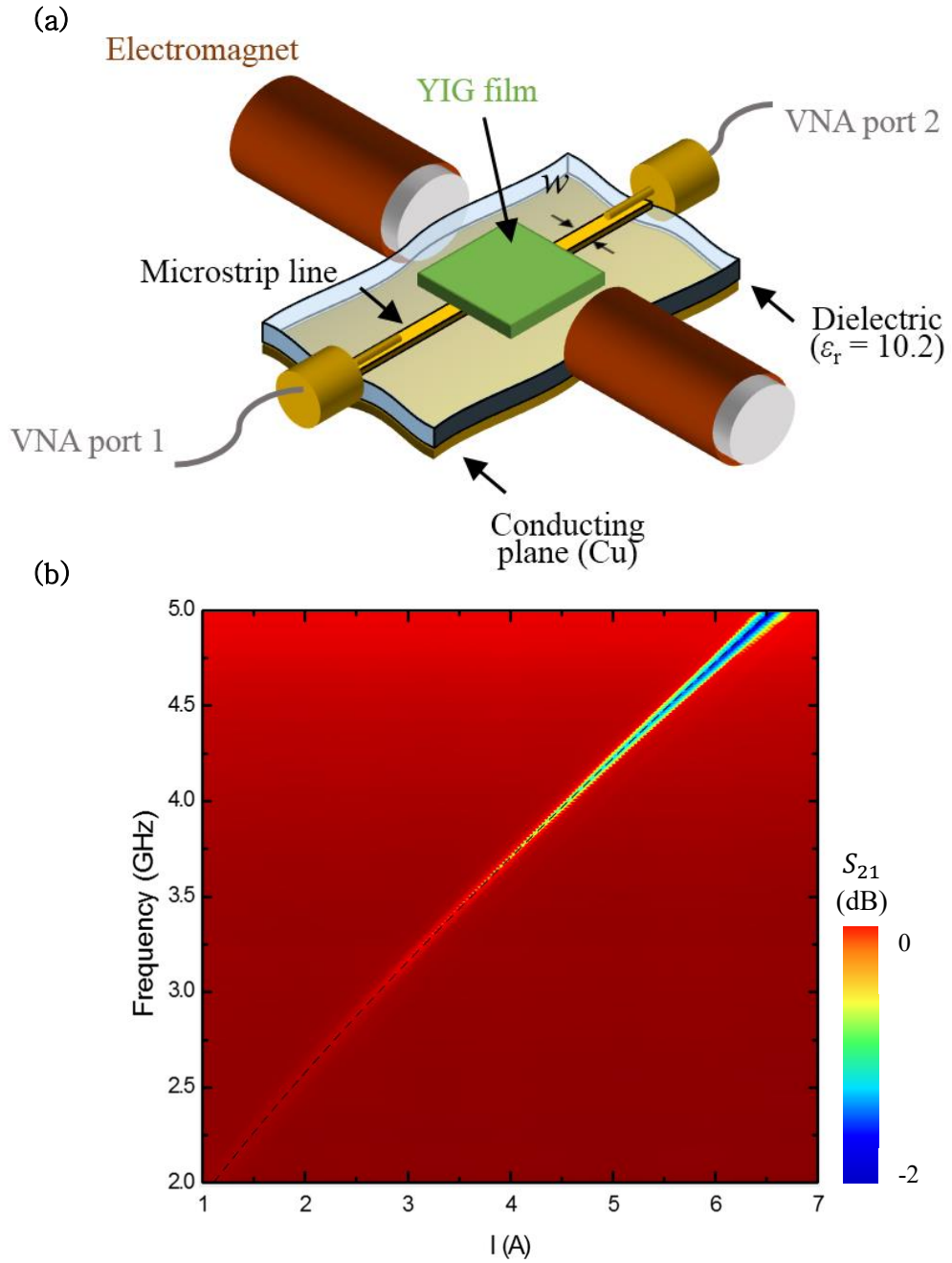
Figure 18. (a) Schematic of the measurement setup. (b) Measured S_{21} parameter of the YIG. Black dotted line is Kittel's mode.

3.2. Network Parameters

3.2.1. Neuron Functions

The fundamental requirement of a hardware neuron in RC is non−linearity. Here, as a function of the magnetic field, or equivalently, as a function of the DC current sent to the electromagnet, three neuron functions are considered: the S_{21} magnitude, frequency, and phase of the lowest S_{21} magnitude point in the S_{21} magnitude measurement of the hybrid system (figure 10.b). Since the waveform sequence is not degenerated, memory is not required, and the neuron function $x_i(t)$ can be simplified as $x(i)$, which is a steady−state function and non−linear as a function of the input.

The lowest S_{21} magnitude point in the $\omega - I$ plane follows the upper (lower) branch before (after) the anti−crossing (AC) point (current value where $\omega_r = \omega_{ISRR}$) as illustrated in figure 11, plotted from equation (2.2.22) with $\omega_c = 4.0GHz$, $\mu_0 H = 0.172T, \alpha = 3.2 \times 10^{-4}, \beta = 2 \times 10^{-2}, \Gamma = 0.04,\ K = 0.05, \delta = 0.5, \varphi = 0$. This is explained by the CMP coefficients η_1 and η_2. The S_{21} magnitude is proportional to the photon proportion of the CMP modes. The S_{21} magnitude is the lowest for the branch containing the most photons,

or equivalently for the branch with the highest coefficient $\boldsymbol{\eta_1}$. As shown in figure 5.c, the upper (lower) branch contains the most photons before (after) AC [44]. Following this explanation, a simple theoretical frequency neuron function was defined from equations (2.2.21) and (2.2.22), where the neuron function follows $\boldsymbol{\omega_+(\omega_-)}$ after (before) anti-crossing.

Unlike an actual time-consuming experiment, the full waveform recognition can be quickly simulated entirely on a computer using previously measured or theoretical neuron functions. Network parameters, such as the number of waveforms and neurons, were chosen from the hybrid system theoretical frequency neuron function.

This simulation method was also used to compare expected results from multiple neuron functions: the measured and theoretical functions of the ISRR alone, YIG alone, and coupled hybrid system.

The software used for experimental or simulation codes is LabVIEW. LabVIEW controls both the DC power supply to encode inputs and the VNA to measure outputs with RS232 and GPIB protocols in the experimental code. LabVIEW also manages all data pre and post-processing.
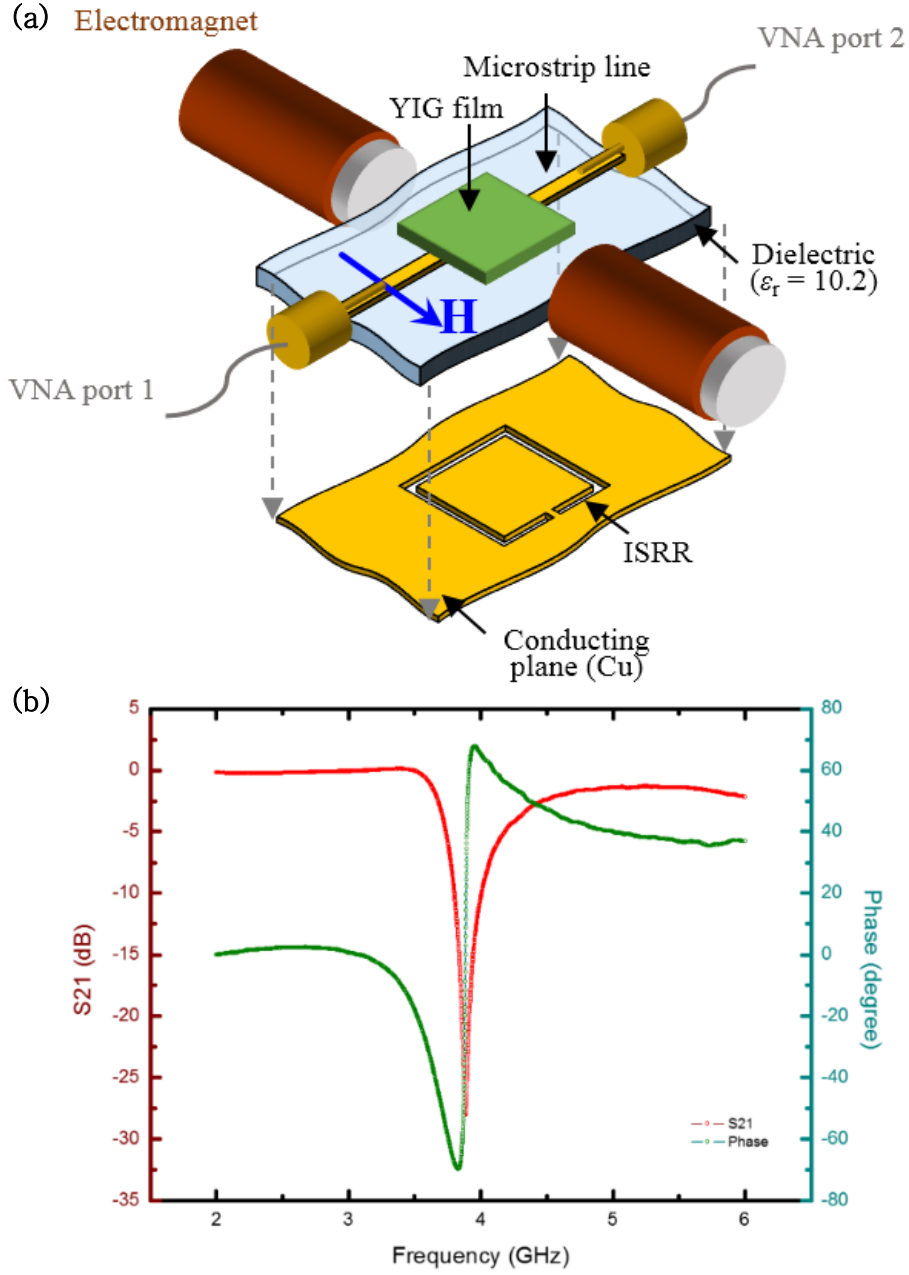
Figure 20. (a) Typical setup for coupling measurement. The magnetic field is perpendicular to the microstrip line. (b) Hybrid system S_{21} magnitude and phase measurement at I=0.25A.
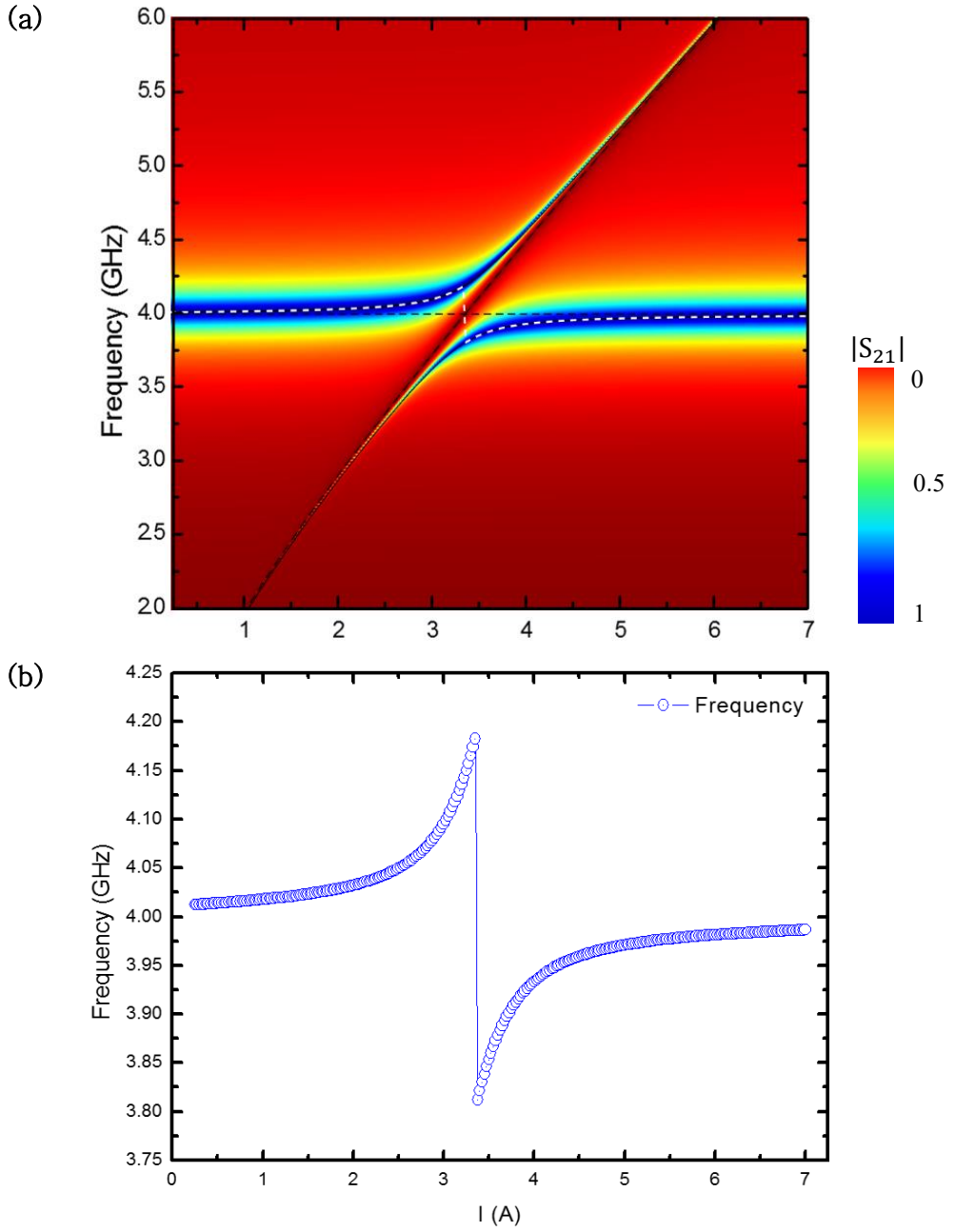
Figure 22. (a) S_{21} norm from equation (2.2.22). White dotted line is the frequency neuron function in the $\omega - I$ plane , dotted and continuous black lines are respectively the magnon, photon, and CMP frequencies. (b) Frequency neuron function.

3.2.2. Inputs and Current center

The random sine and square waveform sequence is created on a computer following the pre-processing method presented in Ch.2 (fig. 12). Each pre-processed data point is encoded in the DC current amplitude sent to the electromagnet, allowing the use of the hybrid system's non-linear neuron functions. The amplitude of square waveforms is 50% higher than sines, with a 1.5A amplitude for squares and 1A for sines. Each waveform is made of 8 sampled points. Since no degeneracies are present between sine and square points, no memories are required for this task. Each DC current value is held 8 seconds. 5 seconds are found to be a minimum required by the electromagnet to reach its steady-state magnetic field value. Because the VNA measures sequentially the S_{21} magnitude and phase, three additional seconds are required by the VNA to perform both sweeps accurately.

Different regions of neuron functions are used depending on the waveform sequence center value. Therefore, the current center is swept through the coupling range, and the whole recognition is done at each current center value. The current center sweep starts at 0.25A, ends at 6.25A, and contains 30 points. The magnetic field time delay prohibits adding more points. To be similar to

experimental results, most simulation results are done with the same

current center sweep.
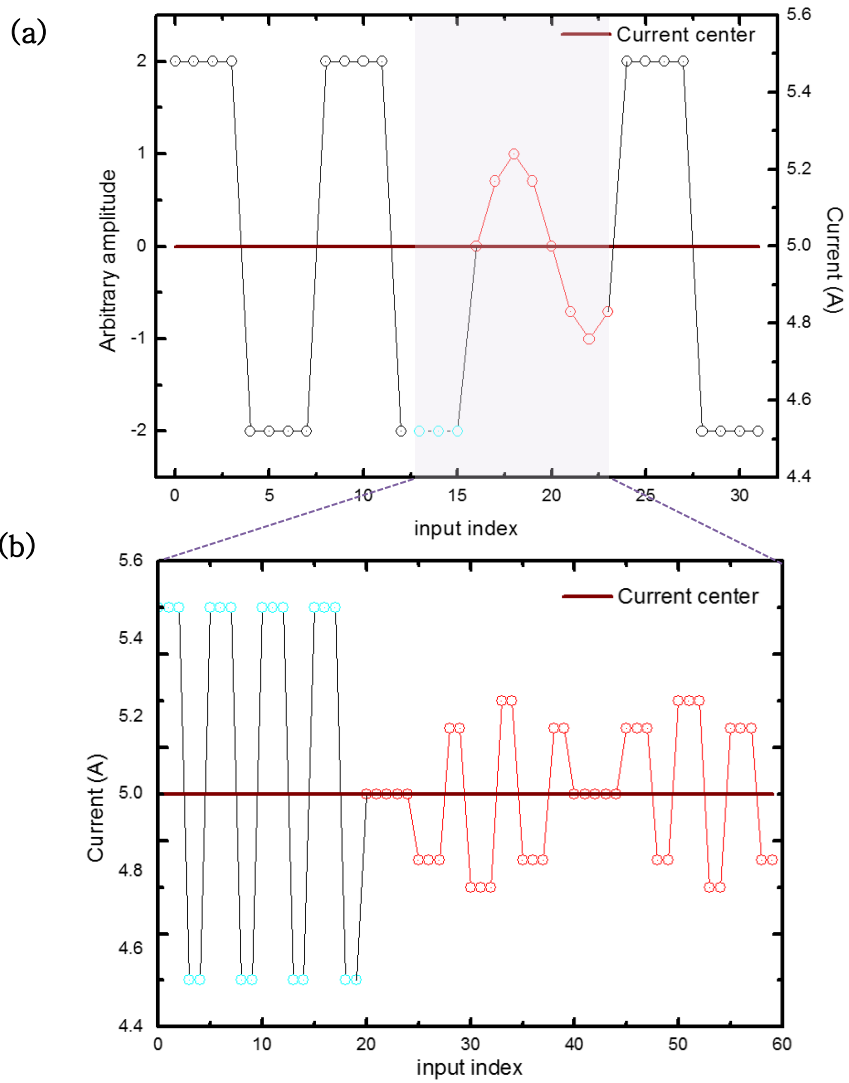
Figure 24. (a) Waveform sequence creation (four shown). (b) Mask multiplication (six neurons shown). Each point is applied as a DC current held 8 seconds.

3.2.3. Neuron and Waveform Number

Experiment execution time t_{exp} is given by $t_{exp} \approx M * n_s * N * * n_I * t_H$, where M is the waveform number, n_s is the number of sampled points per waveform, N is the number of neurons, n_I is the number of current center points and t_H is the magnetic field time delay. The very high t_H value forces the minimization of all the other parameters.

Simulations using theoretical frequency functions showed the success rate and maximum NSE dependences on M and N (figure 13). A minimum threshold value must be given to M and N to successfully perform the recognition and observe peaks of perfect success rates. Once the threshold is crossed, adding more waveforms or more neurons reduces the perfect success rate peaks length. It also does not increase the maximum NSE further, which plateaus around 0.990. From these data, we choose to carry further experiments and simulations with $M = 30$ (15 waveforms for training, 15 for testing), $n_s = 8$, $N = 20$, $n_I = 30$, resulting in $t_{exp} \approx 14$ days long experiments and little simulation execution time.

Simulations for figure 15 were done with $\omega_c = 4.0 GHz, \mu_0 H = 0.172T, \alpha = 3.2 \times 10^{-4}, \beta = 2 \times 10^{-2}, \Gamma = 0.04, K = 0.05, \delta = 0.5, \varphi = 0$.
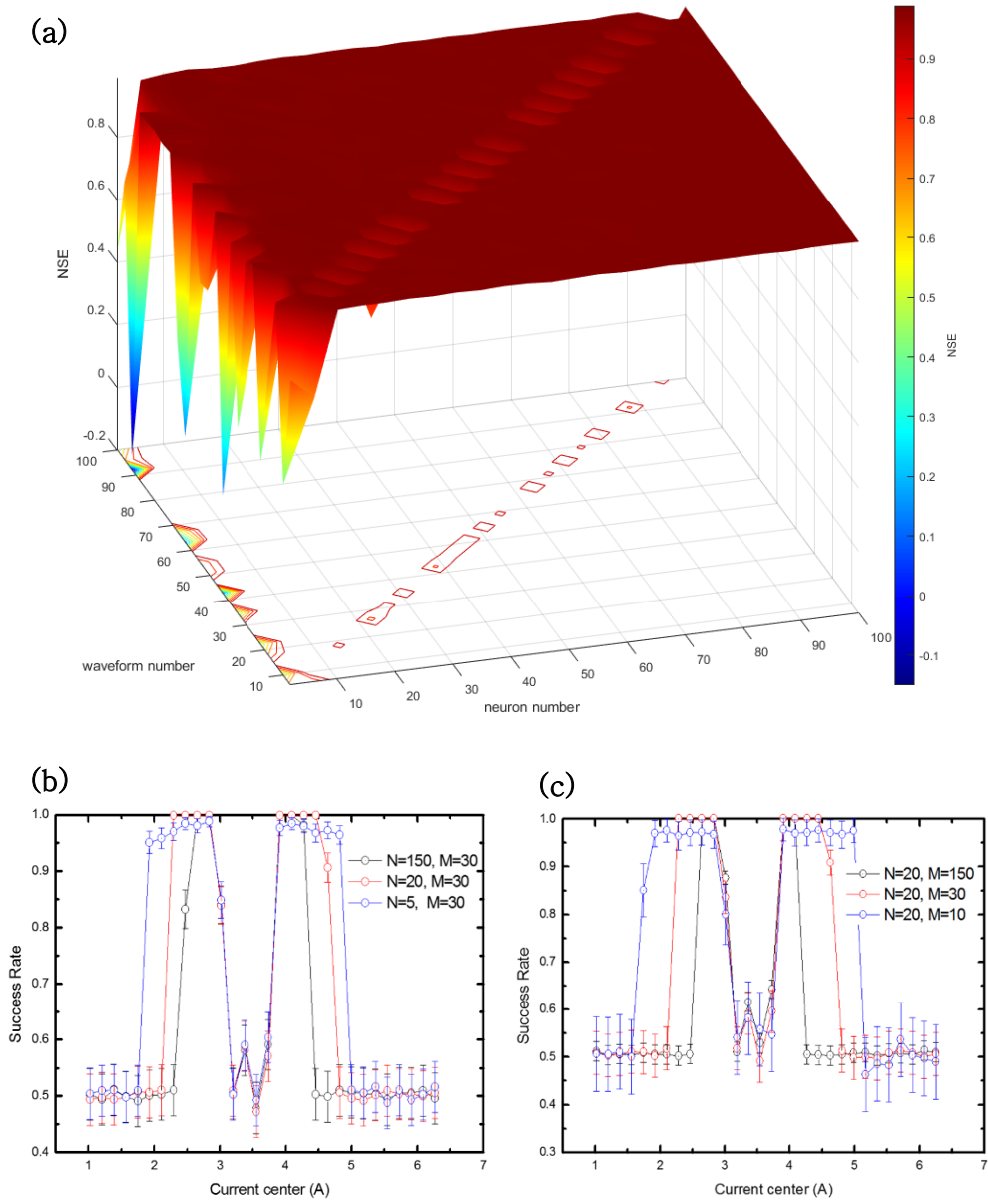
Figure 26. (a) Simulated maximum NSE. (b) Simulated success rate from the frequency function for 30 waveforms. (c) Simulated success rate from the frequency function for 20 neurons.

Chapter 4. Experimental and Simulation Results

4.1. Neuron Functions and Simulation Results

To rapidly compare different systems and configurations, simulations based on measured or theoretical neuron functions were carried out. Experimental ISRR functions, theoretical frequency magnons function, and theoretical frequency hybrid system function were compared, justifying the usage of hybrid system functions over a single cavity or YIG film. Then, two different configurations of in－plane magnetic field angle were compared for experimental hybrid system neuron functions, allowing to find optimal settings for the two weeks long experimental waveform recognition. Only theoretical frequency functions could be obtained by the time the thesis was written.

4.1.1. ISRR Neuron Functions

As a function of the magnetic field, or equivalently, as a function of the DC current sent to the electromagnet, the ISRR S_{21} magnitude, phase, and frequency are constant or weakly varying (figure 14). The S_{21} magnitude presents a small quadratic dependence which is thought to be an artifact from the experimental

setup. The phase has a higher variance and small non−linearities due to measurement and post−measurement calibration imperfections. The frequency is the most stable measurement being almost constant around 4.375 GHz with relatively low variance.

By putting the three experimental neuron functions into a LabVIEW code developed for performing the waveform recognition, according to the method explained in Chapter 2, expected experimental success rates were obtained (figure 14). The S_{21} and frequency functions give respectively weak to completely random (0.5) recognition success rates and cannot be used. This is an expected result since the S_{21} function is weakly varying, and the frequency is almost constant. On the other hand, the phase function leads to a higher success rate for four points. This slightly better result comes from more important but artificial, non−linearities. A perfect phase measurement would be constant at 0 degrees, leading to random success rates (figure 15).

Unless stated otherwise, all simulation results in the thesis use 20 neurons, 30 waveforms 8 sampled points per waveform, and results averaged over 300 simulations.
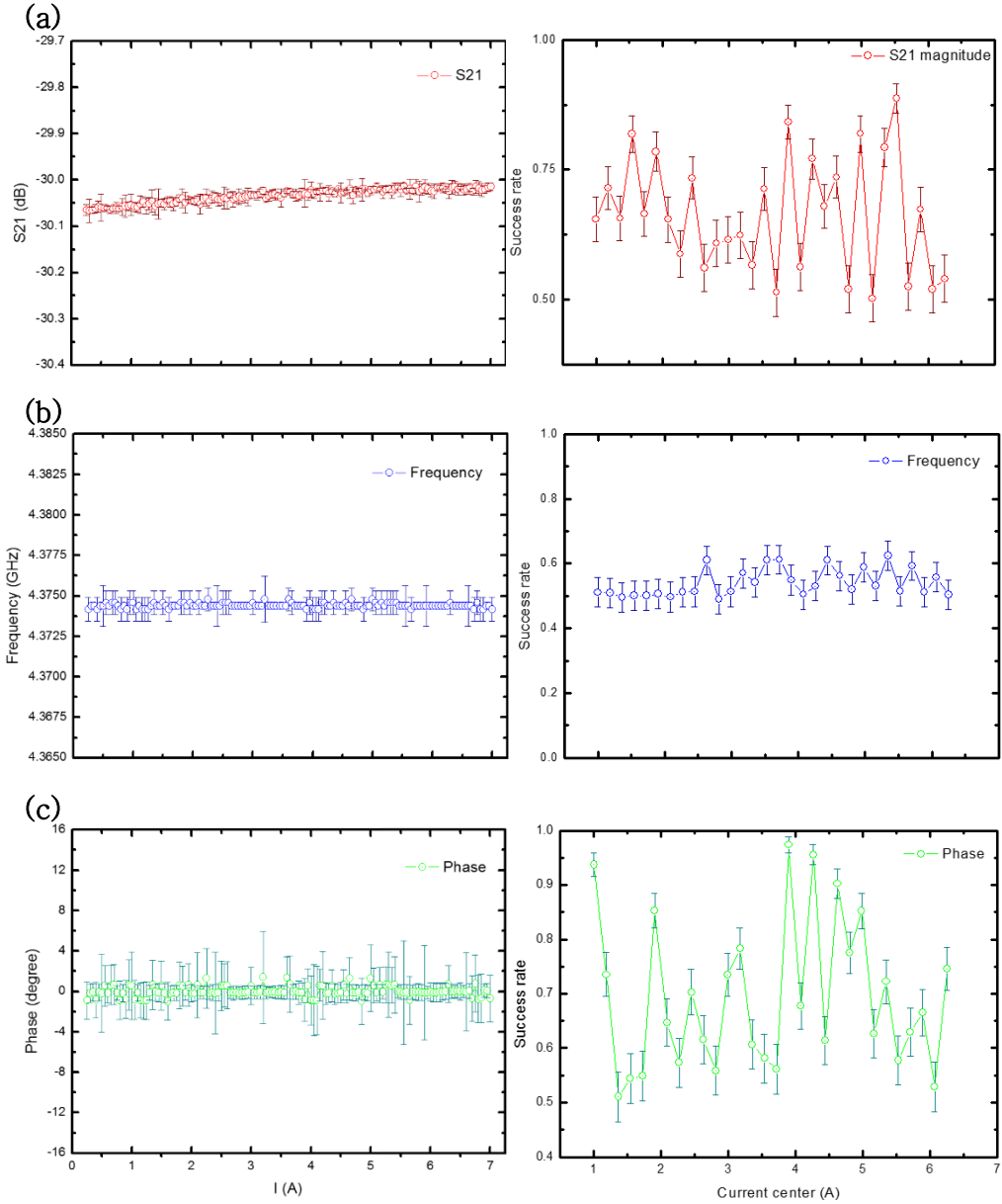
Figure 28. (a) Measured S_{21}, (b) frequency, and (c) phase neuron functions, and their associated expected success rates. Neuron functions values are averaged over three measurements.
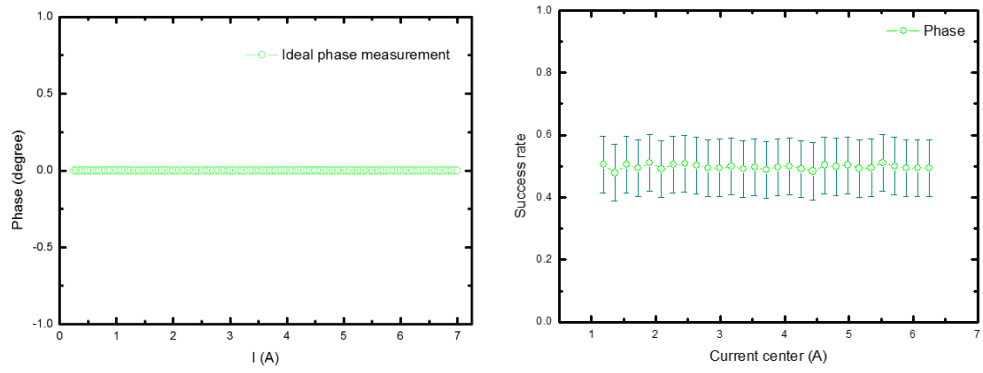
Figure 29. Ideal phase neuron function, and expected success rate.

4.1.2. Magnon Theoretical Frequency Neuron Function

The lowest S_{21} magnitude point for magnons follows Kittel's formula, as shown in figure 9. In general, the magnon dispersion in a YIG film can be written as $\boldsymbol{\omega_{YIG} = \gamma\sqrt{H(H + \mu_0 M_S)} + \delta}$ (4.1.1), with $\boldsymbol{\delta = 0}$ for the Kittel's mode and different otherwise [81] (fig 17.a).

For a given magnetic field value, $\boldsymbol{\omega_{YIG} < 0}$ when $\boldsymbol{\delta < -\gamma\sqrt{H(H + \mu_0 M_S)}}$. Since the current center is swept between 1A and 6.25A and considering the amplitudes of the waveform, neuron functions take values between 0.25A and 6.25A. To avoid negative frequency values in this current range, the minimum $\boldsymbol{\delta}$ value is ≈6.63 GHz.rad. Using the dispersion formula, success rates and NMSE for $\boldsymbol{\delta \in [-6.63, 6.63]}$ GHz were obtained and plotted (fig. 16). Plots show one peak of perfect success, starting at the sweeping range beginning, where the YIG frequency shows a square root curvature. This peak is followed by a range of random success, where the YIG frequency is almost linear. Even if the success peak length tends to decrease as $\boldsymbol{\delta}$ increases, the highest NSE value doesn't change significatively and does not exceed 0.945 (fig.17.b). The highest NSE value was reached at 1A, which is the first swept point.

Theoretical S21 and phase functions could not be obtained by the time the thesis was written.
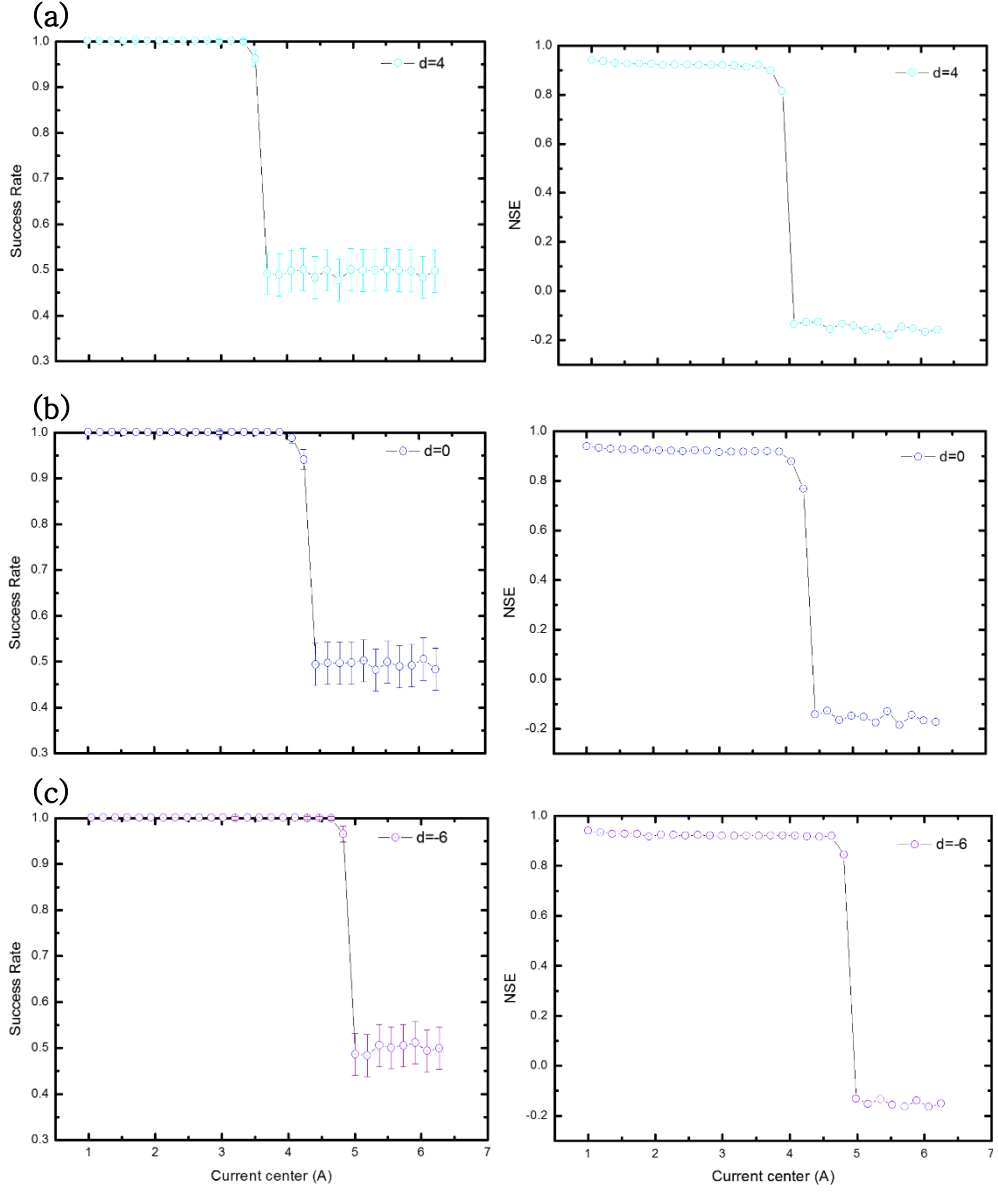
Figure 31. Success rates and NSE from the YIG frequency neuron function for (a) d=4, (b) d=0, (c) d=−6, with d defined as $\mathbf{d} = \boldsymbol{\delta}/\mathbf{1}e\mathbf{9}$.
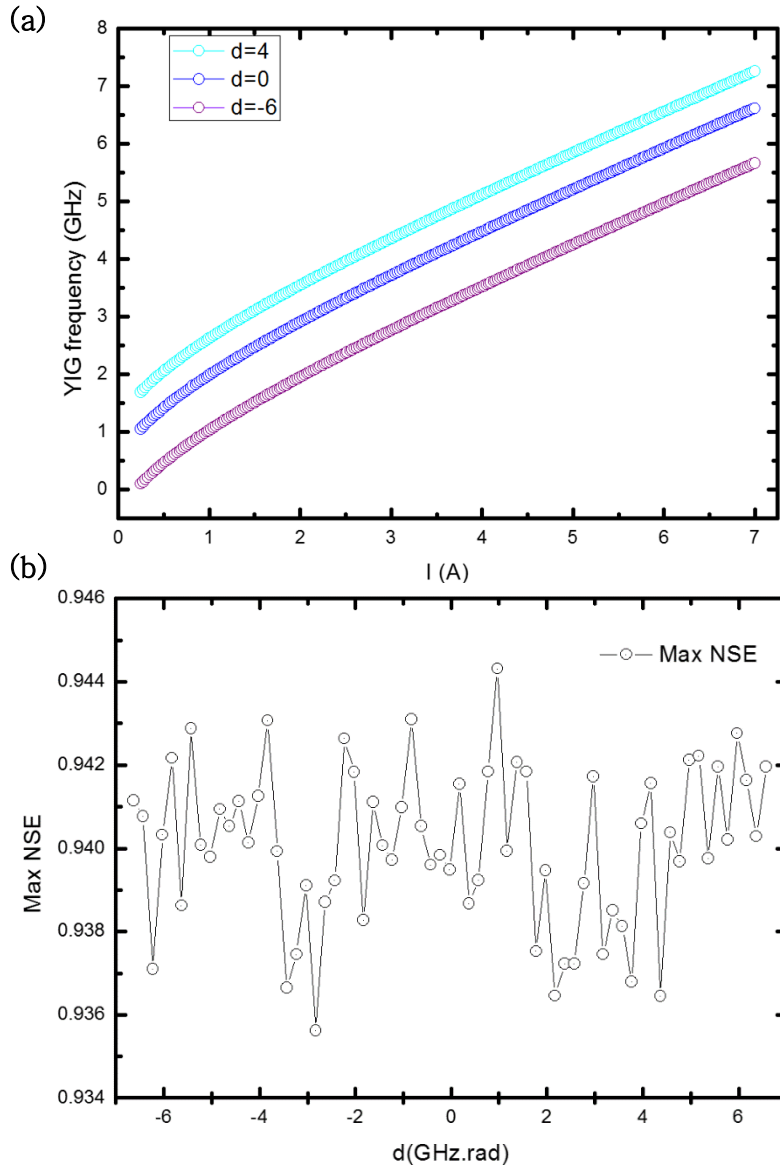
Figure 33. (a) YIG frequency neuron function for d=0,4 and −6. (b) Maximum NSE value reached in the current center sweep. NSE values are averaged over 100 simulations.

4.1.3. Hybrid System Theoretical Neuron Function

Putting the theoretical frequency neuron function in the LabVIEW code ($\omega_c = 4.0GHz$, $\mu_0 H = 0.172T, \alpha = 3.2 \times 10^{-4}, \beta = 2 \times 10^{-2}, \Gamma = 0.04$, $K = 0.05, \delta = 0.5, \varphi = 0$) for different coupling values, K leads to the success rates plotted in figure 18. From these simulation results, we can observe the coupling strength influence on the recognition: as K increases, the two peaks of perfect rates (SR=1) increases in length, and the NSE increases (figure 19.b). The shape of the neuron function can qualitatively explain this observation. As K increases, the non−linear portion of the frequency neuron function increases. MSE values being one order of magnitude lower than magnons and being positively influenced by the coupling strength, computing with AC is more interesting than magnons alone. Theoretical S21 magnitude and phase could not be obtained by the time the thesis was written.
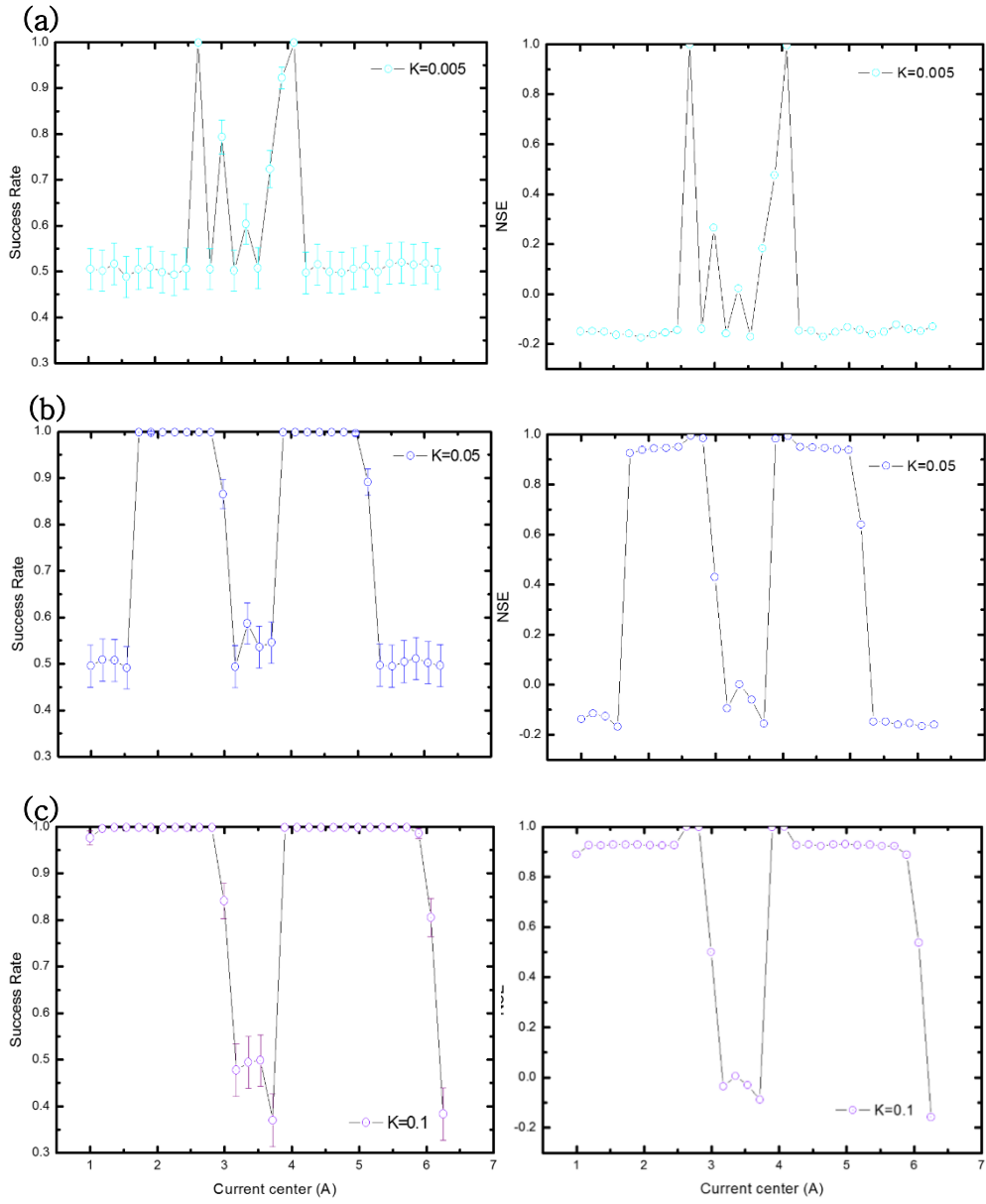
Figure 35. Frequency neuron function and associated simulated success rates for different coupling strength. (a) K=0.005, (b) K=0.05, (c) K=0.

64
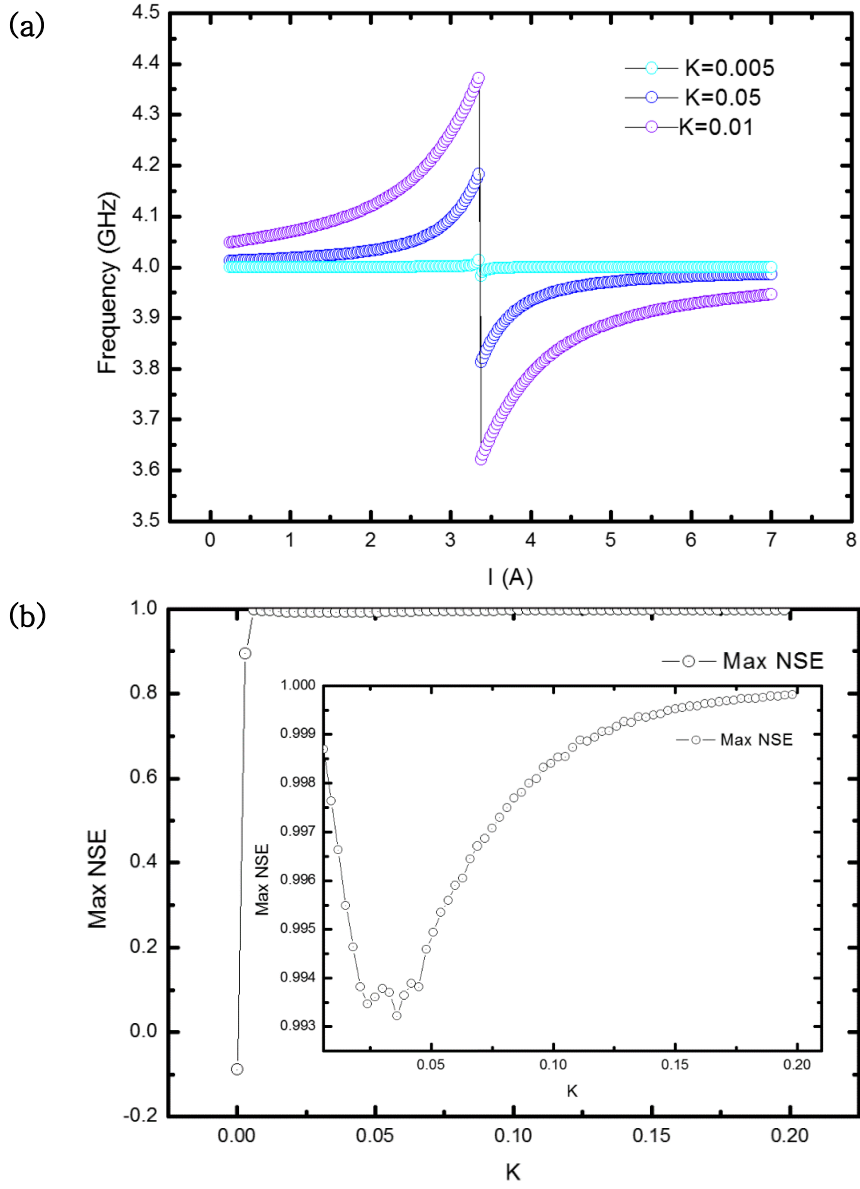
Figure 37. (a) Frequency neuron function for K=0.005,0.05, and 0.01 . (b) Maximum NSE as a function of K. NSE values are averaged over 100 simulations.

4.1.4. Hybrid System Asymmetrical Neuron Functions

Experimental hybrid system functions using the ISRR sample and the YIG film were measured (figure 20). The magnetic field was in the YIG film plane and perpendicular to the microstrip line. To achieve a strong coupling with ISRRs, the YIG film was placed directly in contact with the resonator. Being closer to the ISRR gap and its induced magnetic field, the coupling strength is higher.

Nonetheless, in this configuration and with samples made from this substrate batch, the ISRR resonant frequency changes very sensitively depending on the YIG position. Additionally, the fitting agreement between the S21 magnitude in the $\omega - I$ plane and the frequency dispersion relation varies depending on the YIG position. When the YIG is placed directly over the ISRR gap, the upper branch does not follow the dispersion relation perfectly, whereas the lower branch does. Consequently, the lowest S21 magnitude path, or equivalently, the frequency neuron function, does not follow the upper branch until the anti-crossing point. This is seen by the shift between the frequency function discontinuity (white dotted line) and the anti-crossing point (intersection of black dotted lines) in figure 21.

With the YIG on the ISRR gap, the three experimental neuron functions were put into the LabVIEW code to get simulation results (figure 22). Being asymmetric, the frequency function gives two peaks of perfect success rates, with the second peak being much wider than the first. Surprisingly, the NSE at 1.74A is higher than the NSE of K=0.2, with 0.999968 against 0.99982. The S21 function follows its expected behavior. The S21 magnitude is constant far from anti-crossing and decreases in the coupling region. The multiple discontinuities in the function come from multiple anti-crossings with higher-order spin-wave modes. The phase function follows the same behavior. The phase is constant far from anti-crossing and shows numerous discontinuities in the coupling region. Both S21 and phase success rates show small areas or points of perfect success rate and NSEs lower than the frequency NSE with 0.991433 and 0.970877.

Fitting is done with $\omega_c = 3.7 GHz$, $\mu_0 H = 0.172T$, $K = 0.08, \delta = 0.5, \varphi = 0.$
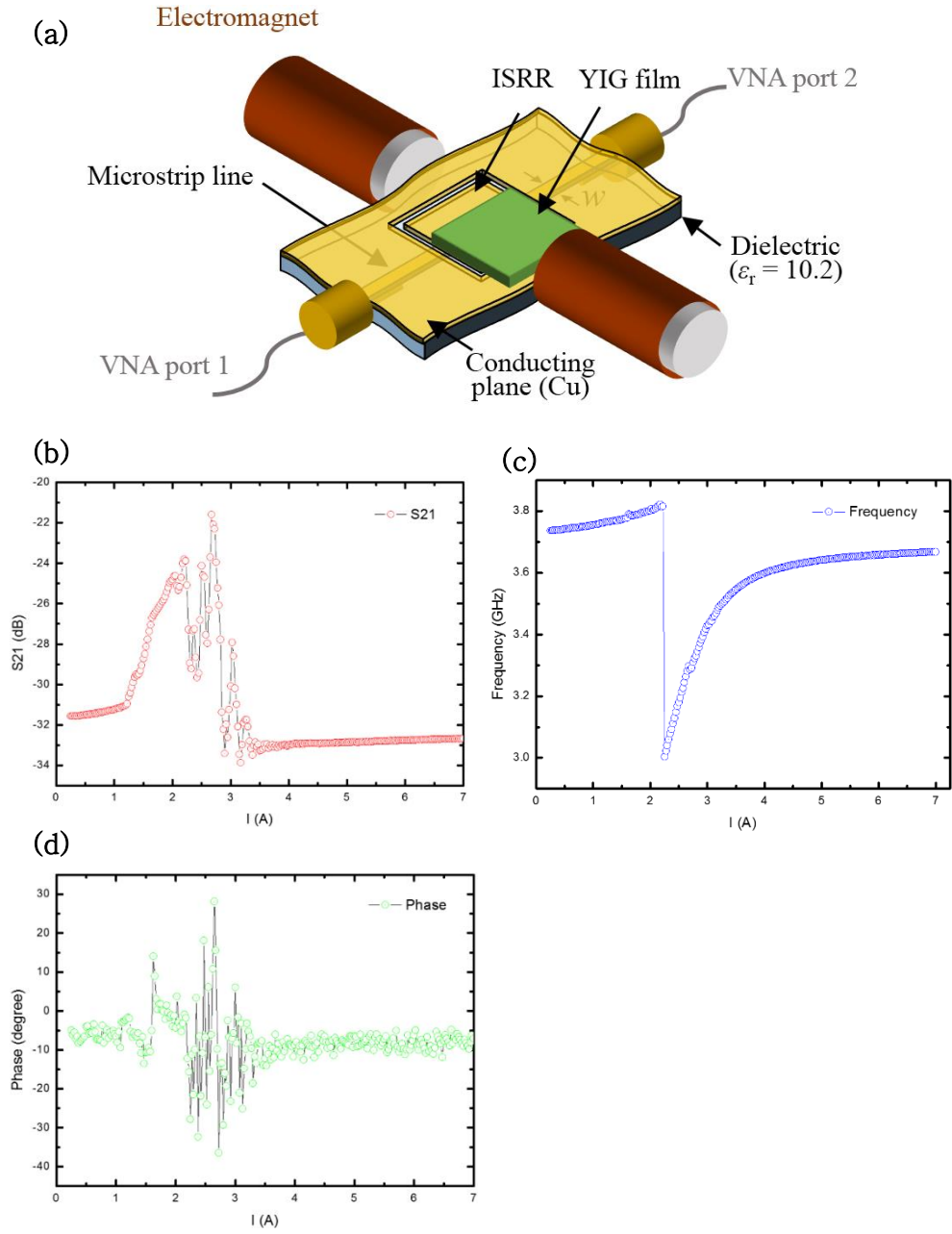
Figure 39. (a) Schematic of the hybrid system. (b) Measured S_{21}, (c) frequency, and (d) phase neuron functions.
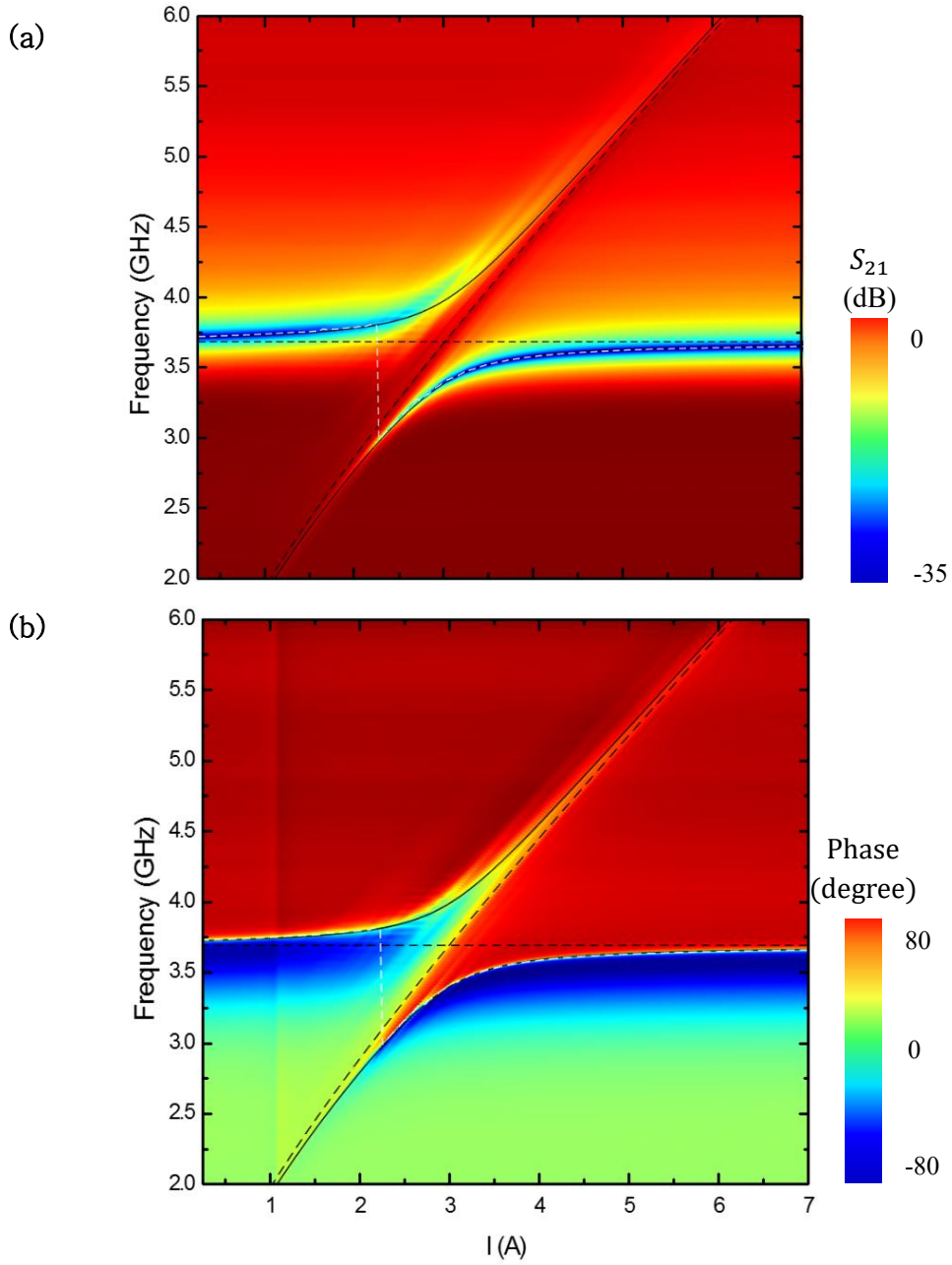
Figure 41. (a) Measured S_{21} magnitude and (b) phase. White dotted line is the frequency neuron function, dotted and continuous black lines are the magnon, photon, and CMP frequencies. The phase shift in the phase plot at 1A is a measurement artifact.
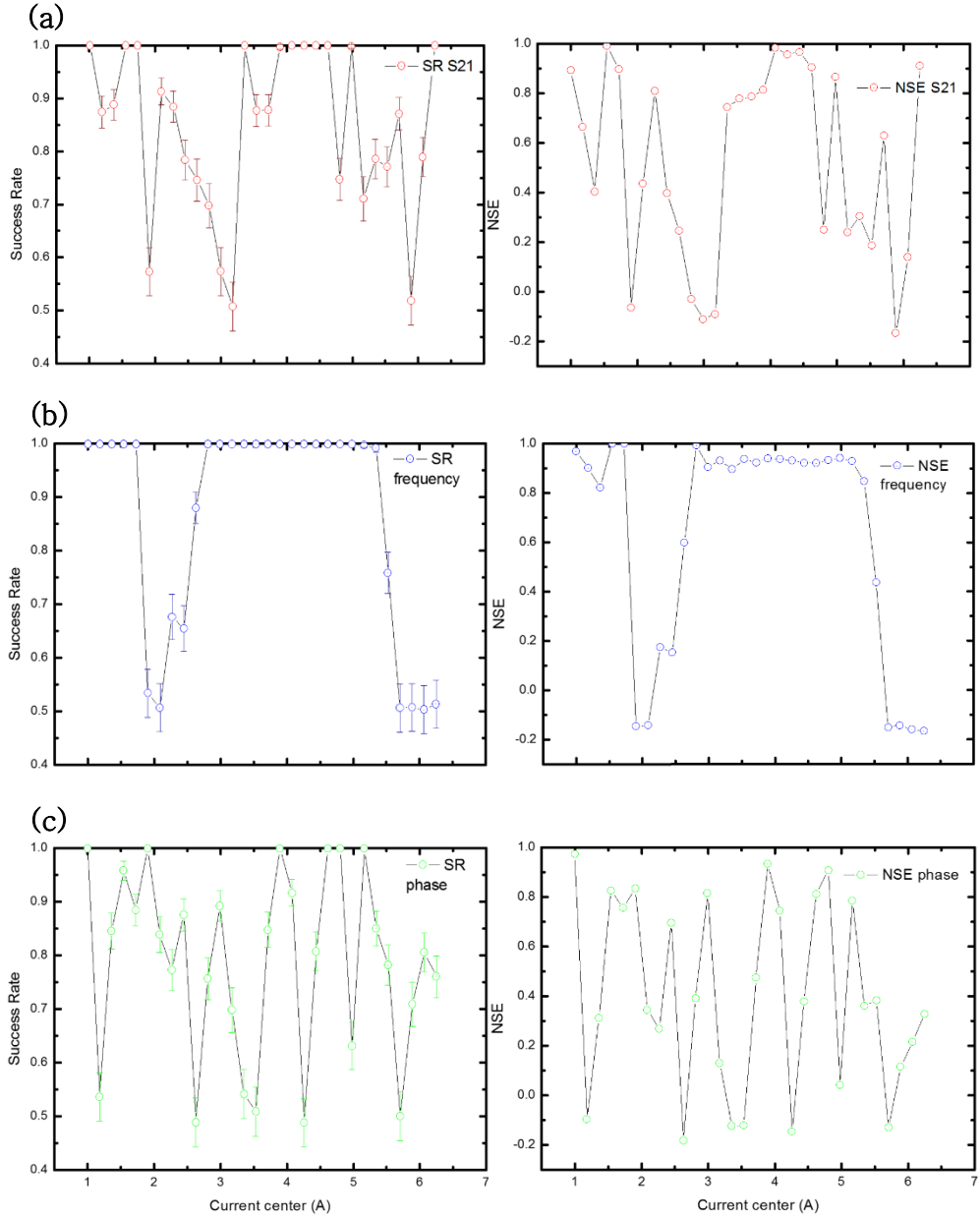
Figure 43. Simulated success rates and NSEs from the measured (a) S_{21}, (b) frequency, and (c) phase neuron functions.

4.1.5. Hybrid System Neuron Functions: 0 degree

The YIG film was carefully placed in the ground plane to maximize the coupling strength and the frequency dispersion fitting agreement (figure 23.a). Consequently, the frequency function becomes closer to the theoretical one, as we can see by the reduced current shift between the dotted white curve discontinuity and the anti−crossing point in Figures 24 and 25. The magnetic field was in the plane of the YIG film and perpendicular to the microstrip line. In this configuration, fine features at the left of Kittel's mode can be observed in figure 24. Those features are higher−order spin−wave modes. Each additional spin−wave mode creates a smaller additional anti−crossing, resulting in additional non−linearities in each neuron function (figure 23). The three functions were put into the LabVIEW code to obtain by simulation the expected experimental results (figure 26). Fitting is done with $\boldsymbol{\omega_c = 4.0GHz}$, $\boldsymbol{\mu_0 H = 0.172T}, \boldsymbol{\alpha =}$ $\boldsymbol{3.2 \times 10^{-4}}, \boldsymbol{\beta = 2 \times 10^{-2}}, \boldsymbol{\Gamma = 0.04}$, $\boldsymbol{K = 0.05}, \boldsymbol{\delta = 0.5}, \boldsymbol{\varphi = 0}$. AC non−linearities in the frequency and S_{21} functions break the first perfect success rate peak into smaller regions of perfect success. Their highest NSE values are respectively 0.99343 at 2.448A and 0.996448 at 1.181A. The phase success rate and NSE are slightly improved, with the highest NSE of 0.990786 reached at 1.36A.
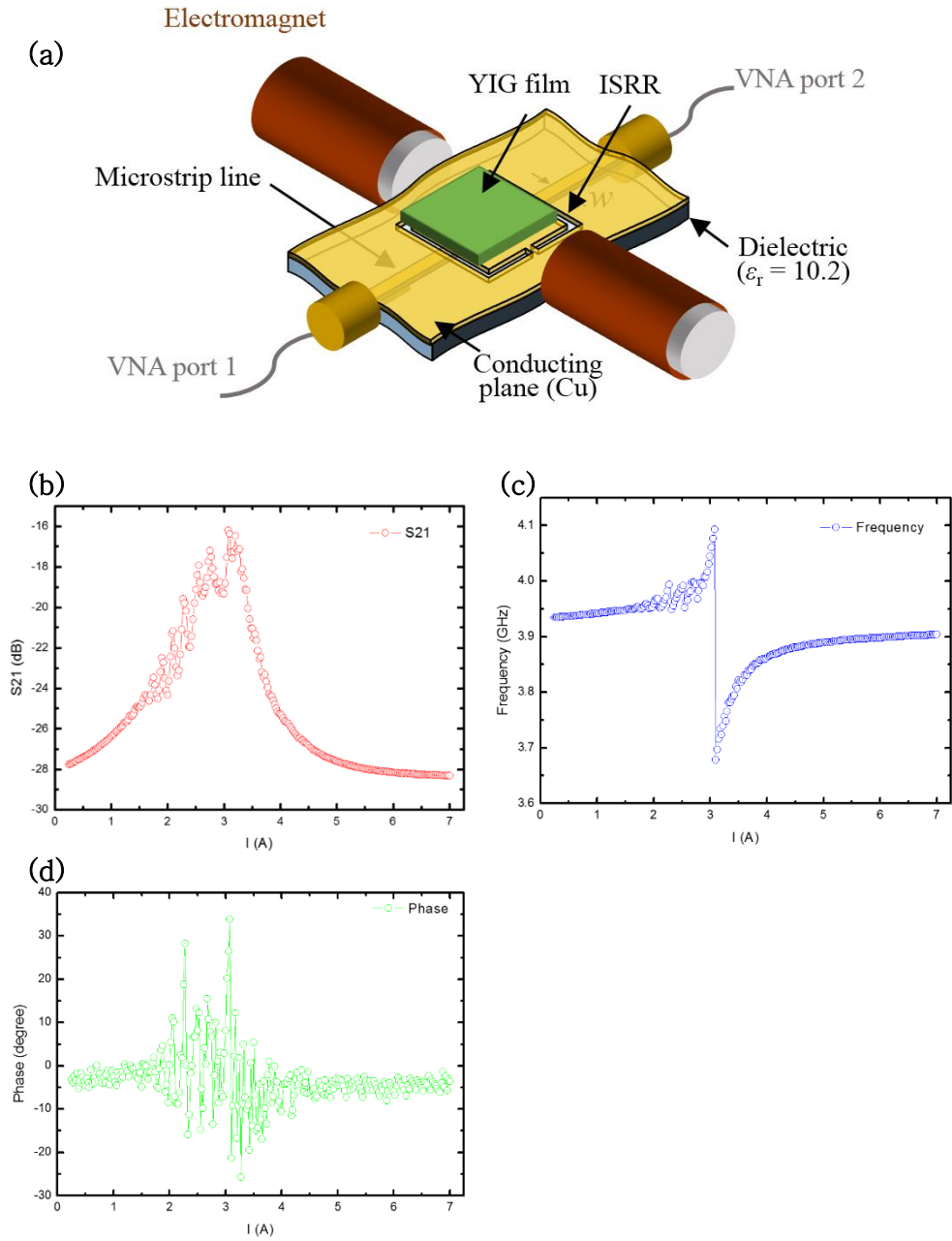
Figure 45. (a) Schematic of the hybrid system. (b) Measured S21, (c) frequency, and (d) phase neuron functions.

Figure 47. (a) Measured **S₂₁** magnitude and (b) phase at 0°. White dotted line is the frequency neuron function, dotted and continuous black lines are the magnon, photon, and CMP frequencies.

73

(a)

(b)

Figure 49. (a) Comparison between experimental and theoretical frequency functions with the fitted CMP dispersion (black continuous lines) and photon and magnon frequencies (horizontal and oblique dotted black lines), and (b) without.

Figure 51. Simulated success rates and NSEs from the measured (a) S_{21}, (b) frequency, and (c) phase neuron functions.

4.1.6. Hybrid System Neuron Functions: 33.5 degree

Anticrossing from higher-order spin-wave modes lowers performances by breaking the ranges of perfect success rate. Nonetheless, it is possible to remove such anti-crossings by changing the in-plane magnetic field angle $\boldsymbol{\varphi}$. B. Bhoi et al. [48] and B. Kim et al. [82] demonstrated in a similar ISRR/YIG hybrid system the existence of a critical angle where all the spin-wave modes have an equal or very close frequency. The critical angle $\boldsymbol{\varphi_c}$ depends on the in-plane magnetic field $\boldsymbol{H}$ according to:

$$\boldsymbol{\varphi_c = \tan^{-1}\sqrt{H\big/_{\mu_0 M_s}}} \qquad (4.1.2)$$

Choosing for $\boldsymbol{H}$ the anti-crossing magnetic field, the critical angle was calculated at $\boldsymbol{\varphi_c = \tan^{-1}\sqrt{H\big/_{\mu_0 M_s}} = \tan^{-1}\sqrt{0.076\big/_{0.172}} \approx}$ $\boldsymbol{33.65}°$. After setting the magnetic field accordingly, the three neuron functions were measured and put into the LabVIEW code (figure 27). The S21 and frequency first success peaks are now continuous or almost. The frequency success peaks are smaller in length owing to smaller coupling strength as the angle $\boldsymbol{\varphi}$ increases, as shown by Bhoi et al. [48]. The number of points of high phase success rate remains almost unchanged. Maximum NSEs are getting lower with 0.991815 at 2.45A, 0.98469 at 2.63A, and 0.968879 at

4.80A for the frequency, S21, and phase functions, respectively (figure 30), indicating slightly lower performances. As opposed to 0 degree, anti-crossing with higher-order modes almost does not happen, making the data clearer (figure 28). Therefore, even if the maximum expected NSE values are lower than at 0 degrees, this configuration has been chosen to get the first experimental results. Additionally, the fitting between the theoretical and experimental frequency function is improved (figure 29).

Fitting is done with $\omega_c = 3.88GHz$, $\mu_0 H = 0.172T$, $K = 0.045, \delta = 0.45, \varphi = 0.$
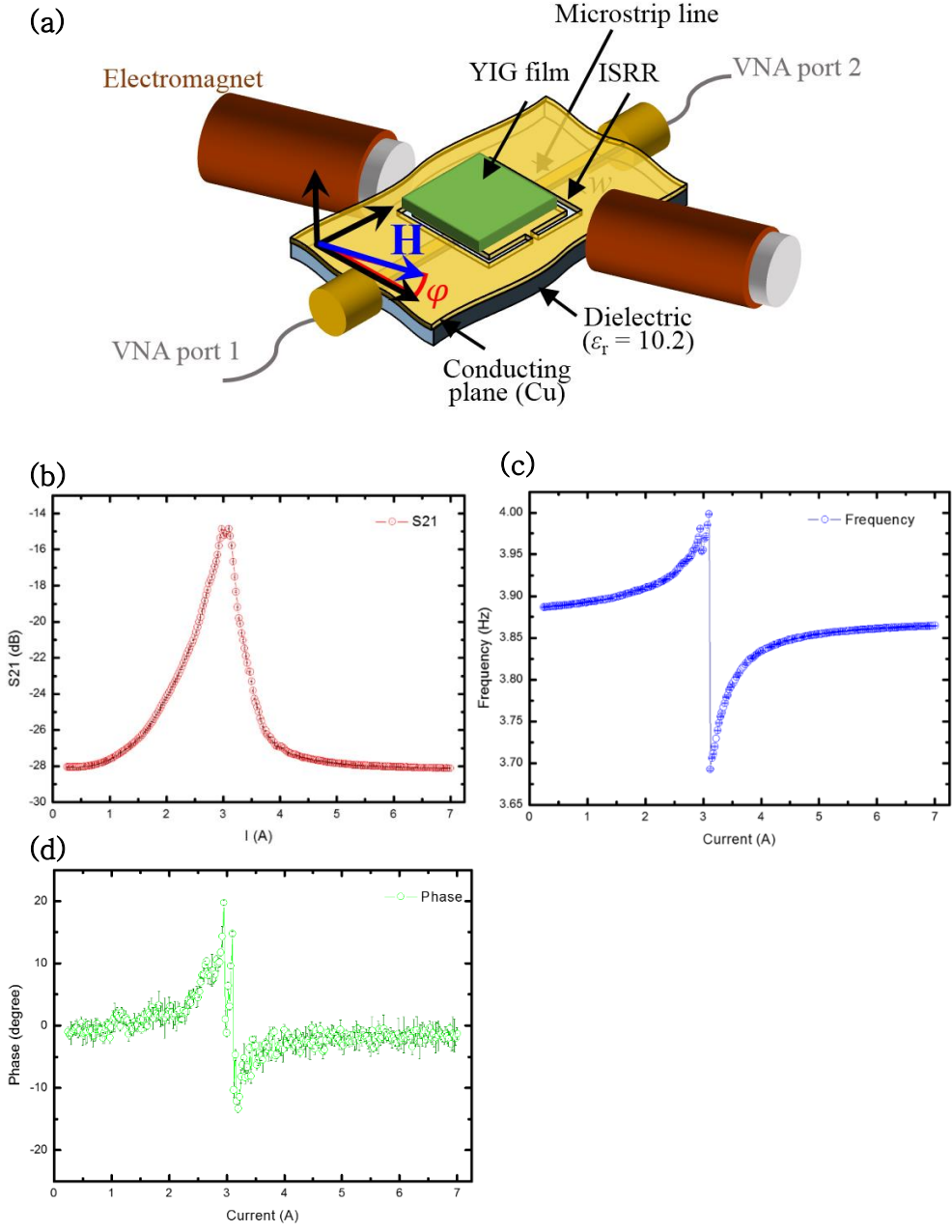
Figure 53. (a) Schematic of the hybrid system at φ_c. (b) Measured S_{21}, (c) frequency, and (d) phase neuron functions.
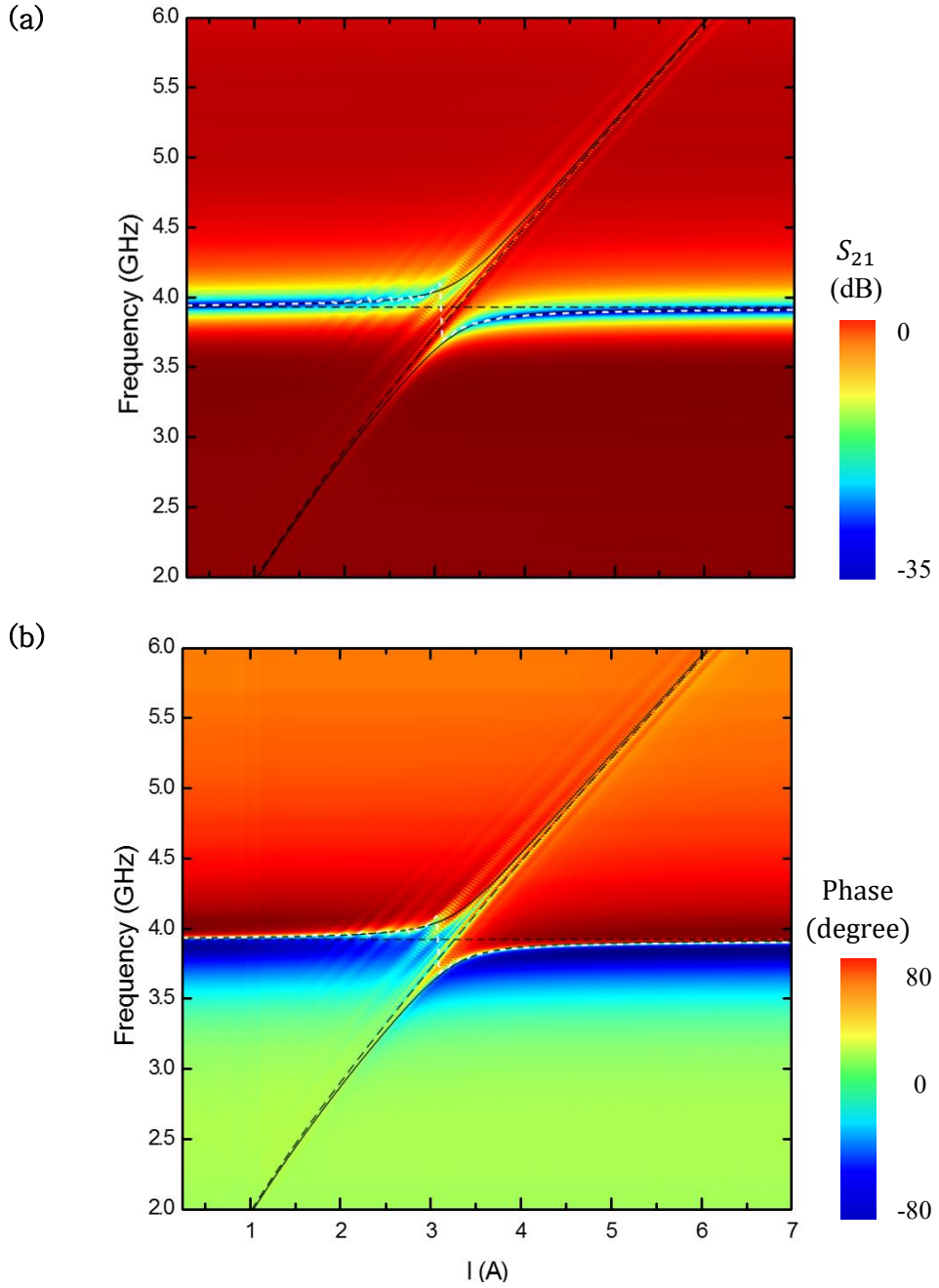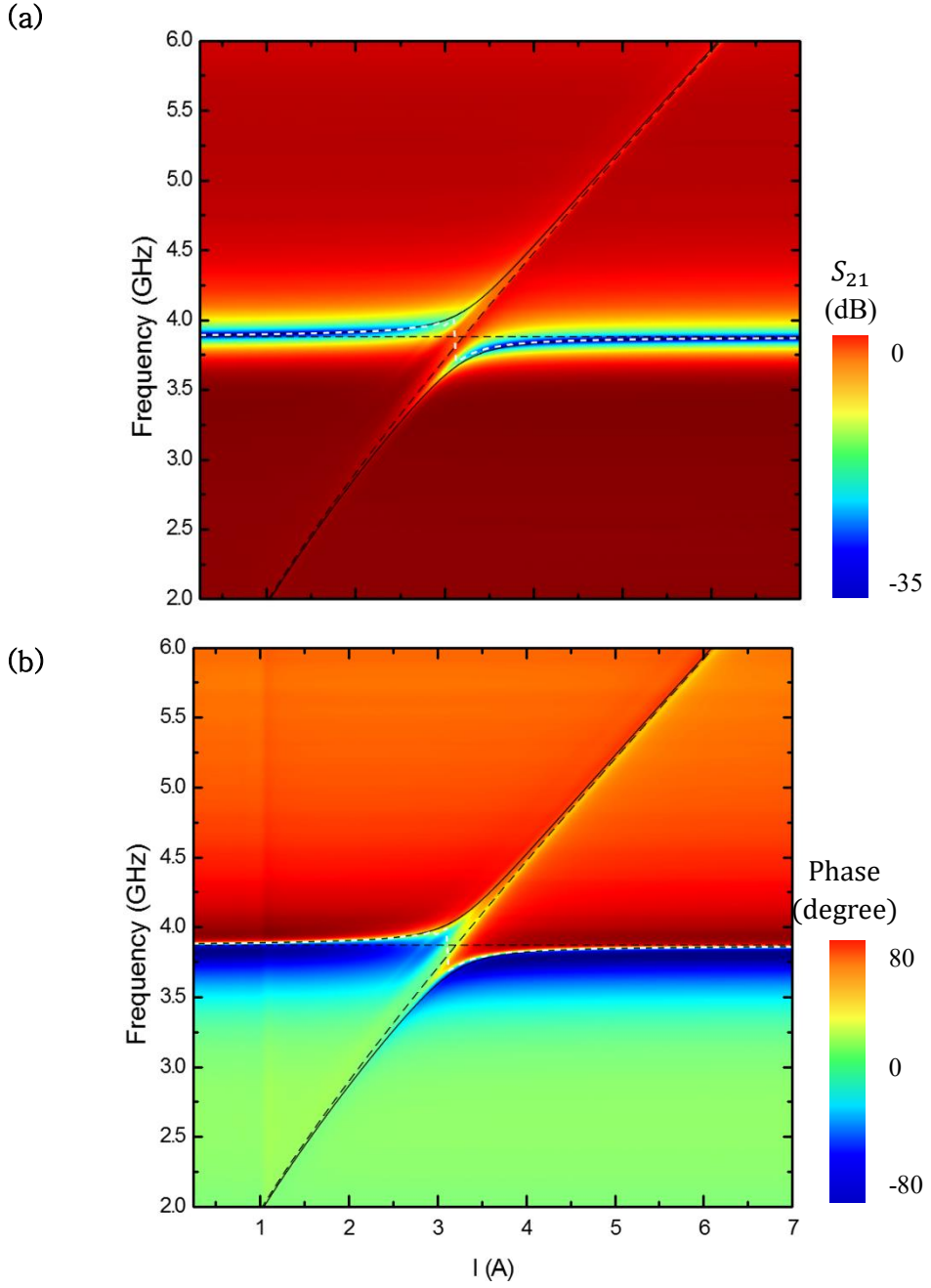
Figure 55. (a) Measured S_{21} magnitude and (b) phase at φ_c. White dotted line is the frequency neuron function, dotted and continuous black lines are the magnon, photon, and CMP frequencies.
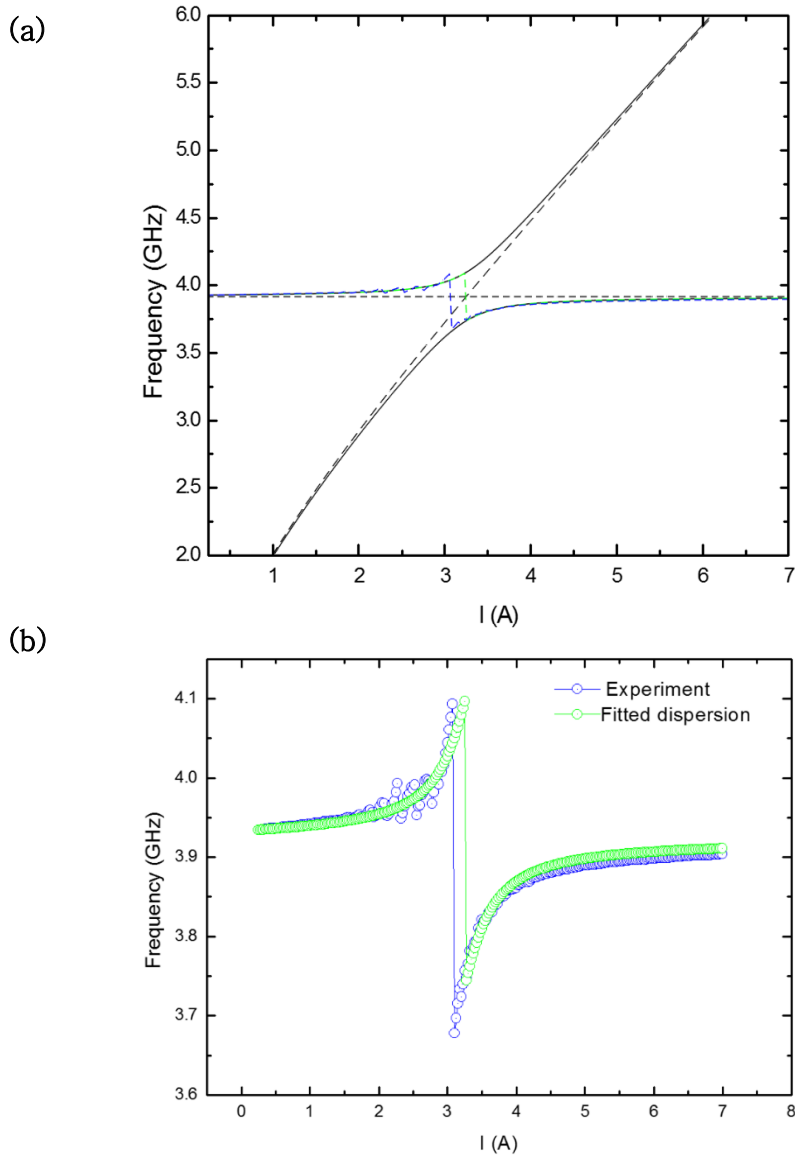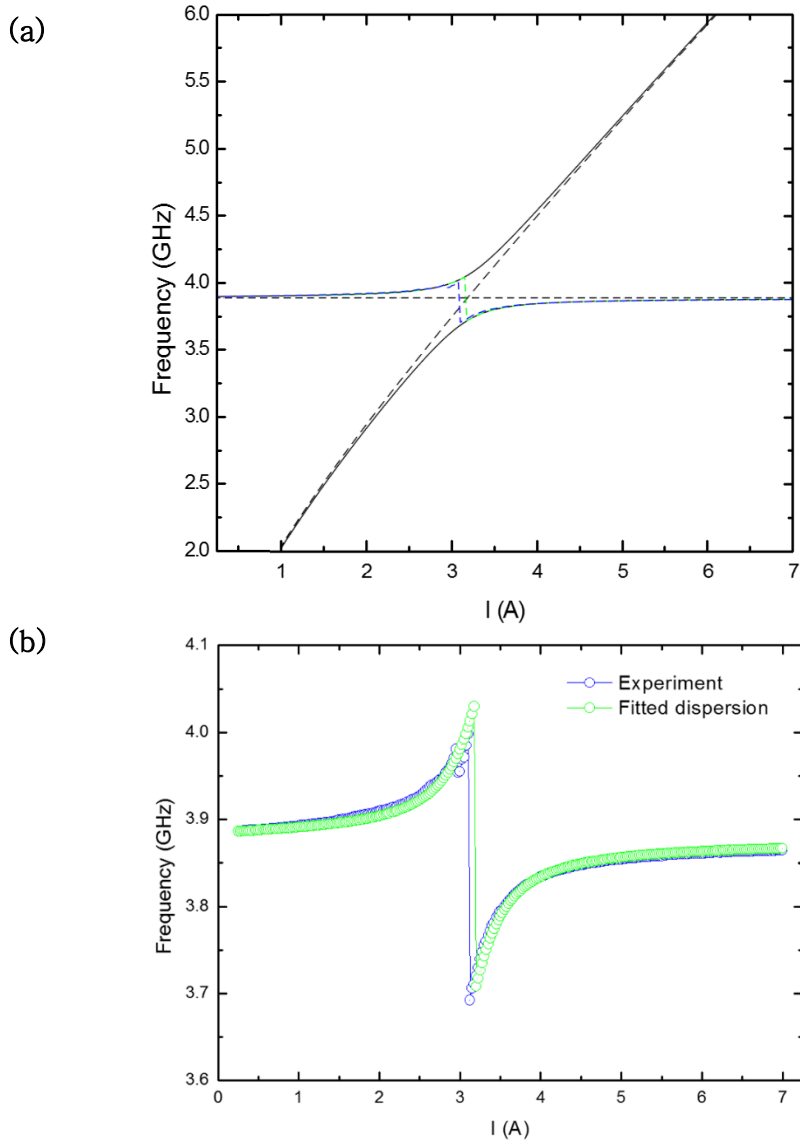
Figure 57. (a) Comparison between experimental and theoretical frequency functions with the fitted CMP dispersion (black continuous lines) and photon and magnon frequencies (horizontal and oblique dotted black lines), and (b) without.
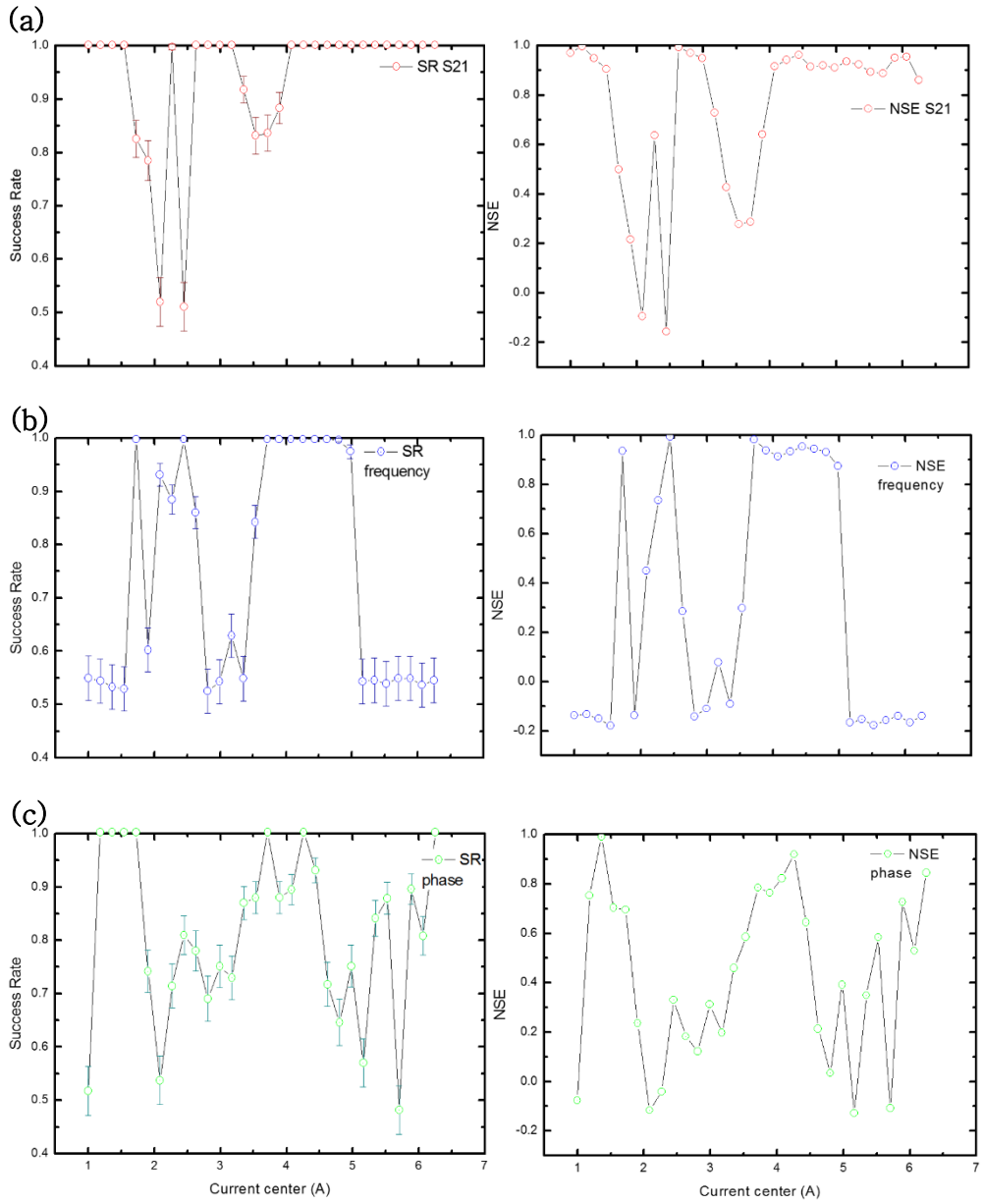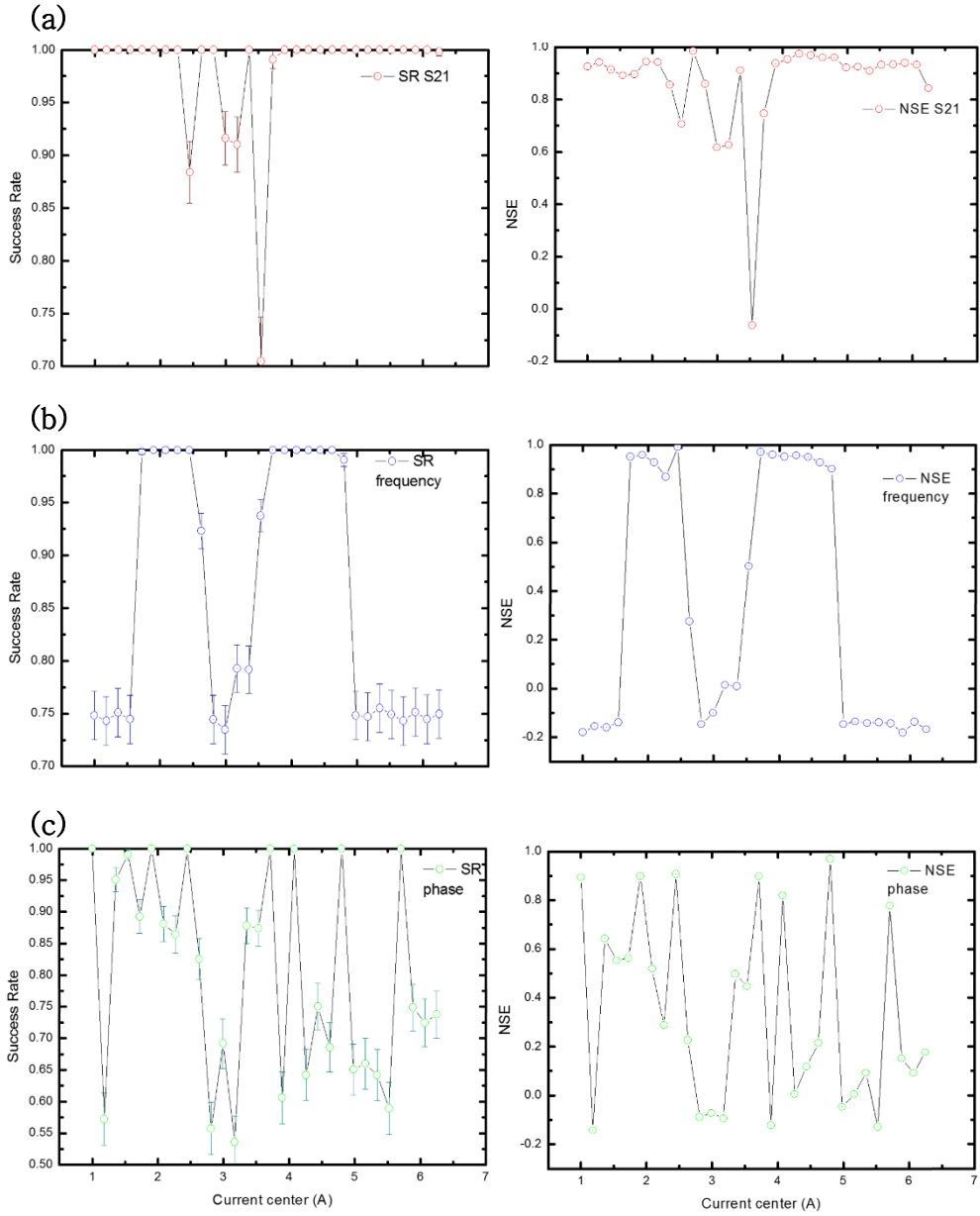
Figure 59. Simulated success rates and NSEs from the measured (a) S_{21}, (b) frequency, and (c) phase neuron functions at φ_c.

4.2. Experimental Success Rates

Experimental success rates were obtained for the hybrid system at the critical angle. Previous success rates from the frequency function of another sample for a low and high coupling strength are also presented.

4.2.1. Success Rates and NSE at the critical angle

Experimental success rates (figure 31) from the S_{21} magnitude and frequency are in good agreement with simulation results. The maximum NSE is 0.991658 at 2.63A for the S_{21} function and 0.990555 at 2.45A for the frequency function. Phase results are slightly below expected with only three points of perfect success rate, and a maximum NSE of 0.9546209 at 3.89655A against seven predicted points of perfect success and a 0.968879 predicted maximum NSE value. This discrepancy is thought to come from the higher variance in phase measurement. Those results successfully demonstrate waveform recognition with the S21 magnitude, frequency, and phase of photon－magnon coupling in an ISRR/YIG film hybrid system.
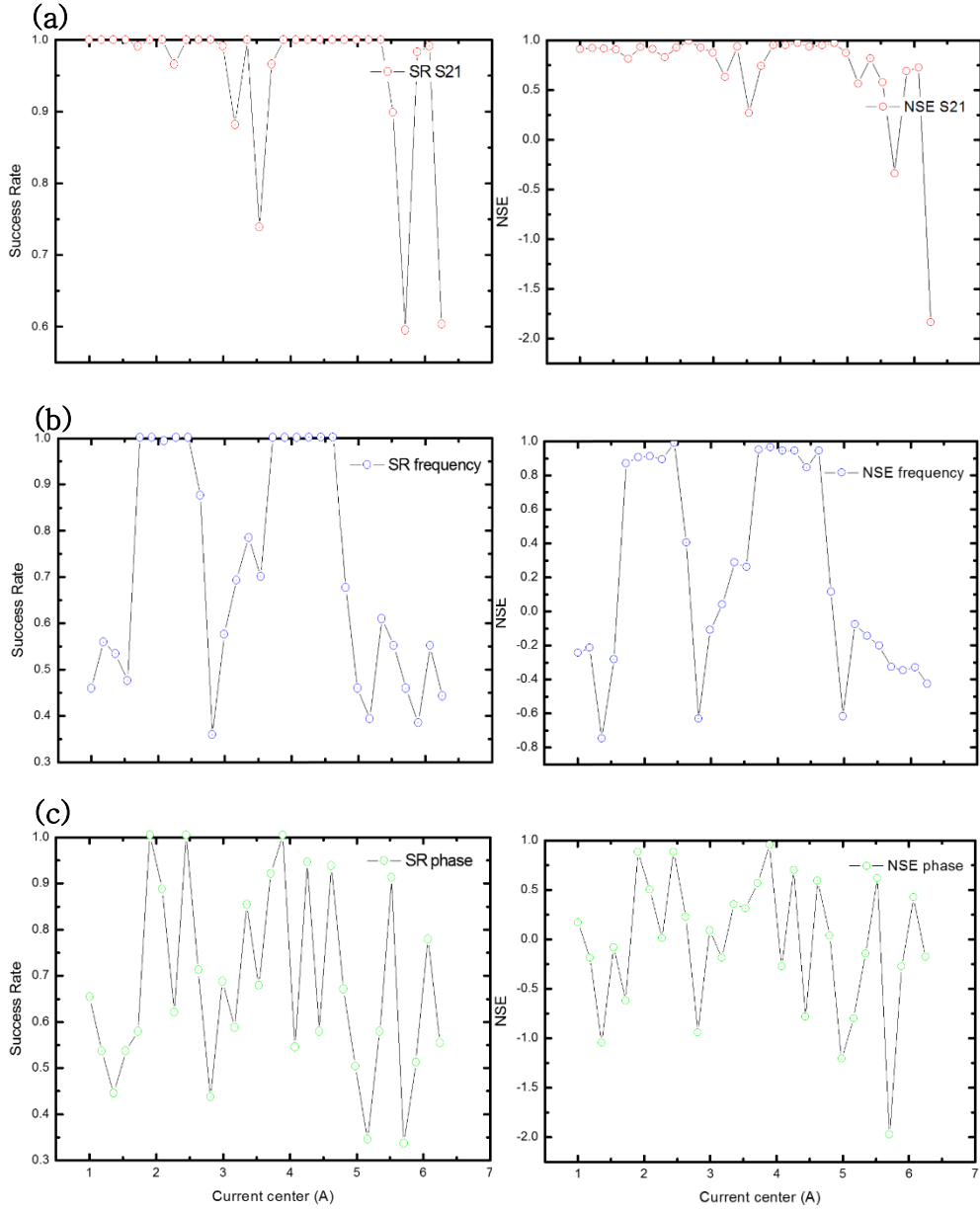
Figure 61. Experimental success rates and NSEs from the (a) S_{21}, (b) frequency, and (c) phase neuron functions at φ_c.

4.2.2. Frequency Success Rates for 2 YIG positions

Experimental comparison of different coupling strengths was partially obtained from another ISRR sample (figure 32). The 4GHz sample was used in references [45] and [48]. The YIG film was either on the microstrip line above the ISRR (weak coupling) or directly on the ISRR gap (very strong coupling). The magnetic field was in-plane and perpendicular to the microstrip line ($\boldsymbol{\varphi = 0}$ degree). Despite putting the YIG film directly on the ISRR gap, this sample's frequency function was symmetric. Only experimental frequency success rates were obtained from the sample before breaking. S21 and phase neuron functions for the YIG on the ISRR gap were measured and had a similar shape and expected results to the 4.375GHz sample shown in parts **4.1.5** or **4.1.6**. Experimental results follow simulations well. As the coupling increases, peaks of perfect or close to a perfect success rate increase in length. Discrepancies between simulation and experimental results for the weak and strong coupling positions are respectively coming from suboptimal VNA settings (low IF BW) and additional non-linearities coming from anti-crossings with higher-order spin-wave modes. Simulations are done with $\boldsymbol{\omega_c = 3.88 GHz}$, $\boldsymbol{\mu_0 H = 0.172T, \alpha = 3.2 \times 10^{-4}, \beta = 2 \times 10^{-2}, \Gamma = 0.04, \ \delta = 0.5, \varphi = 0}$.
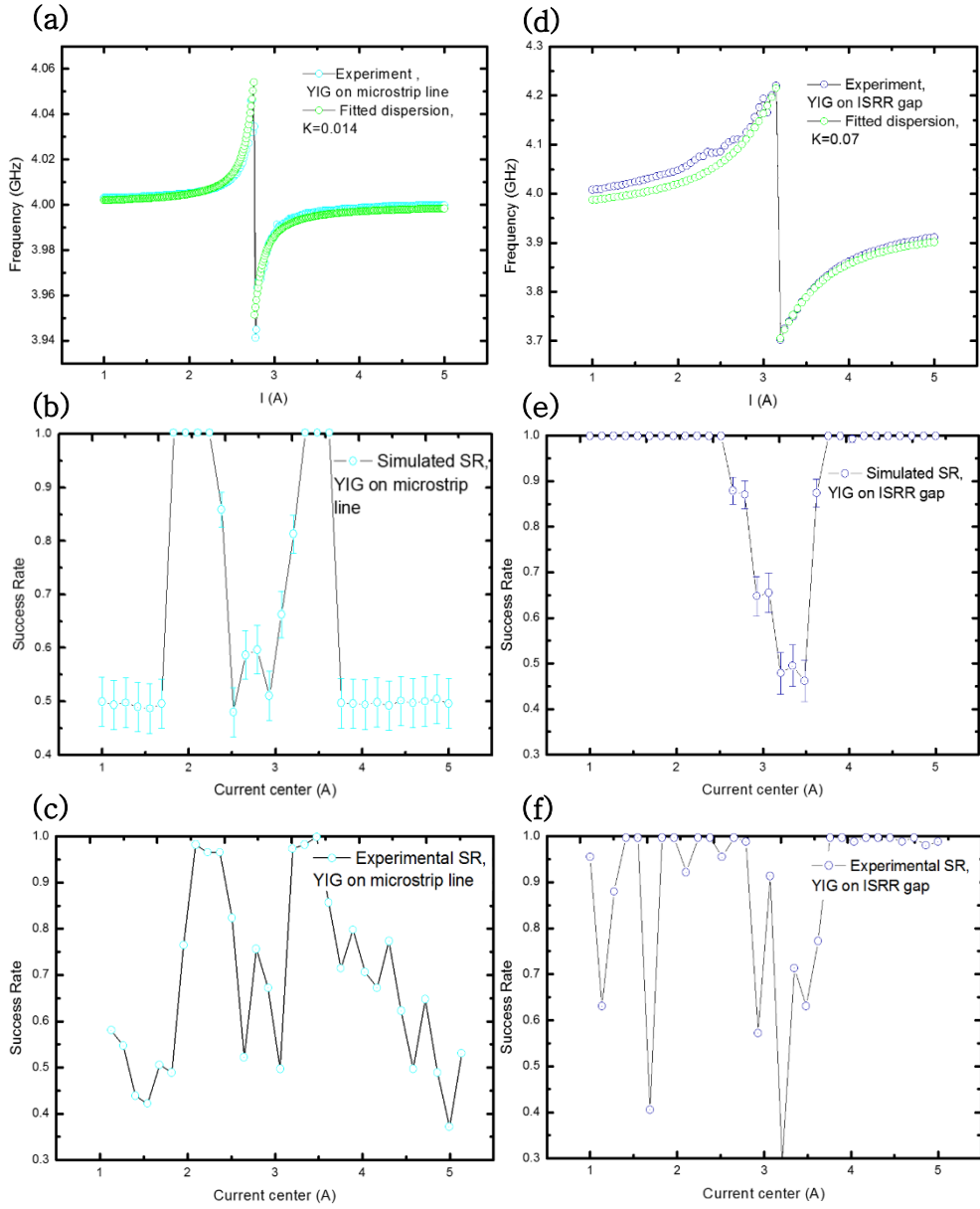
Figure 63. Experimental and theoretical frequency functions for (a) the YIG on the microstrip line, and (d) on the ISRR gap. Simulated success rate for (e) K=0.014 and (b) K=0.07. Experimental success for (c) the YIG on the microstrip line, and (f) on the ISRR gap.

Chapter 5. Concept of Vowel Recognition with Photon−Magnon Coupling

5.1. Recognition with STNOs

An STNO is a nanometric pillar made up of two ferromagnetic layers separated by an oxide tunneling layer. The magnetization of the first layer is pinned by exchange interaction and acts as a spin polarizer, whereas the magnetization of the second layer is free [87]. After tunneling, the spin−polarized current from a DC source exerts a torque on the free layer magnetization, resulting in magnetic moments precession. The combination of Spin−Transfer Torque (STT) and magnetoresistance effects converts the magnetic oscillations into measurable voltage oscillations [88].

M. Romera et al. showed that a network composed of 4 electrically coupled STNOs could perform vowel recognition [27], [86]. A current source independently controls the resonant frequency of each STNO voltage oscillations (I_1 to I_4, figure 33.b.). Since the STNOs are connected in series and no current is equal to 0, the frequencies are different and increasing from left to right ($f_{STNO1} < f_{STNO2} < f_{STNO3} < f_{STNO4}$). Network outputs are the resonant frequencies red with a spectrum analyzer (figure 33.c).

Seven different vowels are used in their first demonstration. Thirty－seven women pronounce each vowel. Every vowel is encoded in a pair of 2 distinct frequencies, linear combinations of characteristic sampled frequencies. The two frequency coordinates f_A and f_B are generated by two RF current generators, and both circulate in a stripline above the STNO array. The resulting input vowels can be represented in a 2－dimensional plane, as shown in figure 33.f. Recognition relies on synchronization. An STNO can lock its frequency onto an external microwave current frequency if frequencies are close enough (figure 33.d). When two microwave frequencies f_A and f_B are applied to the system, the resulting synchronization states can be represented in a 2－dimensional map (figure 33.e). The recognition consists in associating seven different synchronization states to the seven different vowels. If the network is trained, reading the synchronization state allows seeing which vowel has been applied to the system. The training starts from a random map (random values of I_1 to I_4) and the goal is to converge to the preselected map by tuning the currents. The learning algorithm adjusts the currents to minimize the frequency difference between the targeted and input frequencies. State of the art success rate was obtained (figure 34).
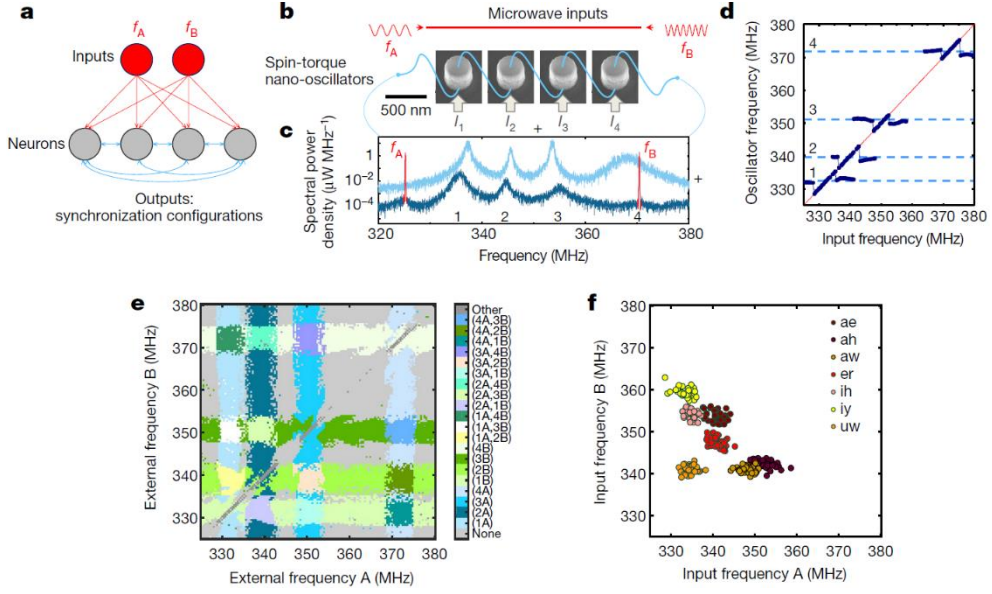
Figure 64. (a) Schematic of the network. (b) Schematic of the experimental setup. (c) Output without (light blue), and with (dark blue) inputs. (d) STNOs synchronization. (e) Synchronization map. (f) Vowels. [27]
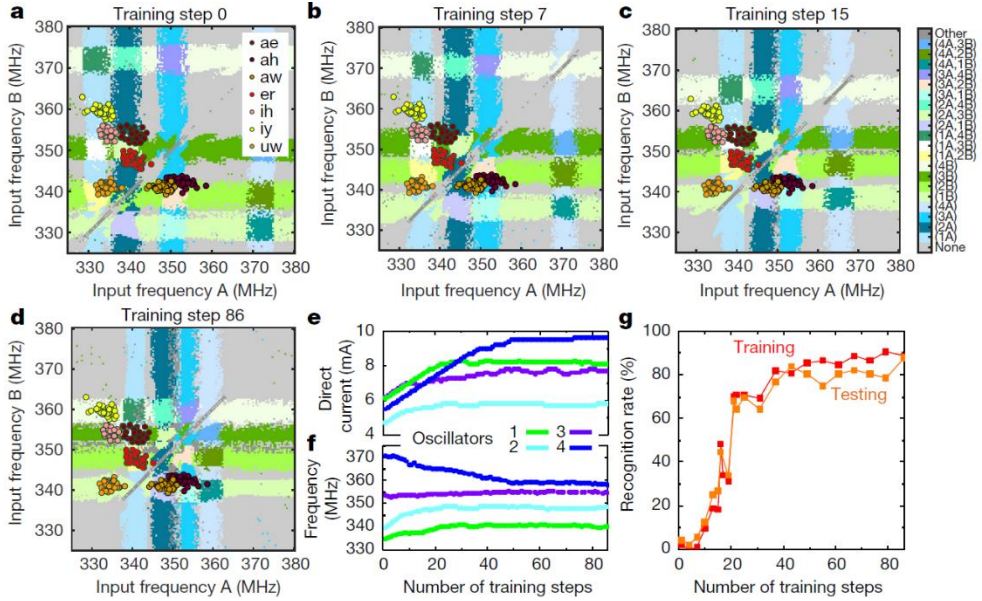
Figure 65.(a) Random starting coupling map. Map after (b) seven steps, (c) 15 steps. (d) Final map. (e) current, and (f) frequency evolution. (g) Success rates. [27]

5.2. Recognition with Photon−Magnon Coupling

The concept can be readily translated to PM coupling. An array of in−plane SRRs loaded with varactor diodes (v−SRR) [89] gives voltage−tunable oscillators corresponding to the current−tunable STNOs (fig. 35.a). An YIG film in contact with the v−SRRs gives PM coupled states corresponding to the synchronization states between the STNOs and one microwave frequency f_A (fig 35.b). The coupling state is red with a VNA. The difficulty is encoding f_B. In the translated concept, f_A is the magnon frequency coming from the YIG film and controlled by an external magnetic field H_A. Since f_A and f_B must be controlled independently, adding a second YIG film and a second magnetic field H_B requires H_A and H_B to affect independently their respective YIG film, which is hard to achieve in practice. An alternative is to use the v−SRR physics to our advantage. In the non−linear regime of a v−SRR [90]−[92], the resonator frequency can be tuned by both the frequency and power of the pump (fig 35. b,c,d). Adding a second microwave current to the sample allows encoding f_B through either the pump power or frequency. Here, success rates benefit from high coupling strengths: the coupling ranges increase, reducing misclassification.
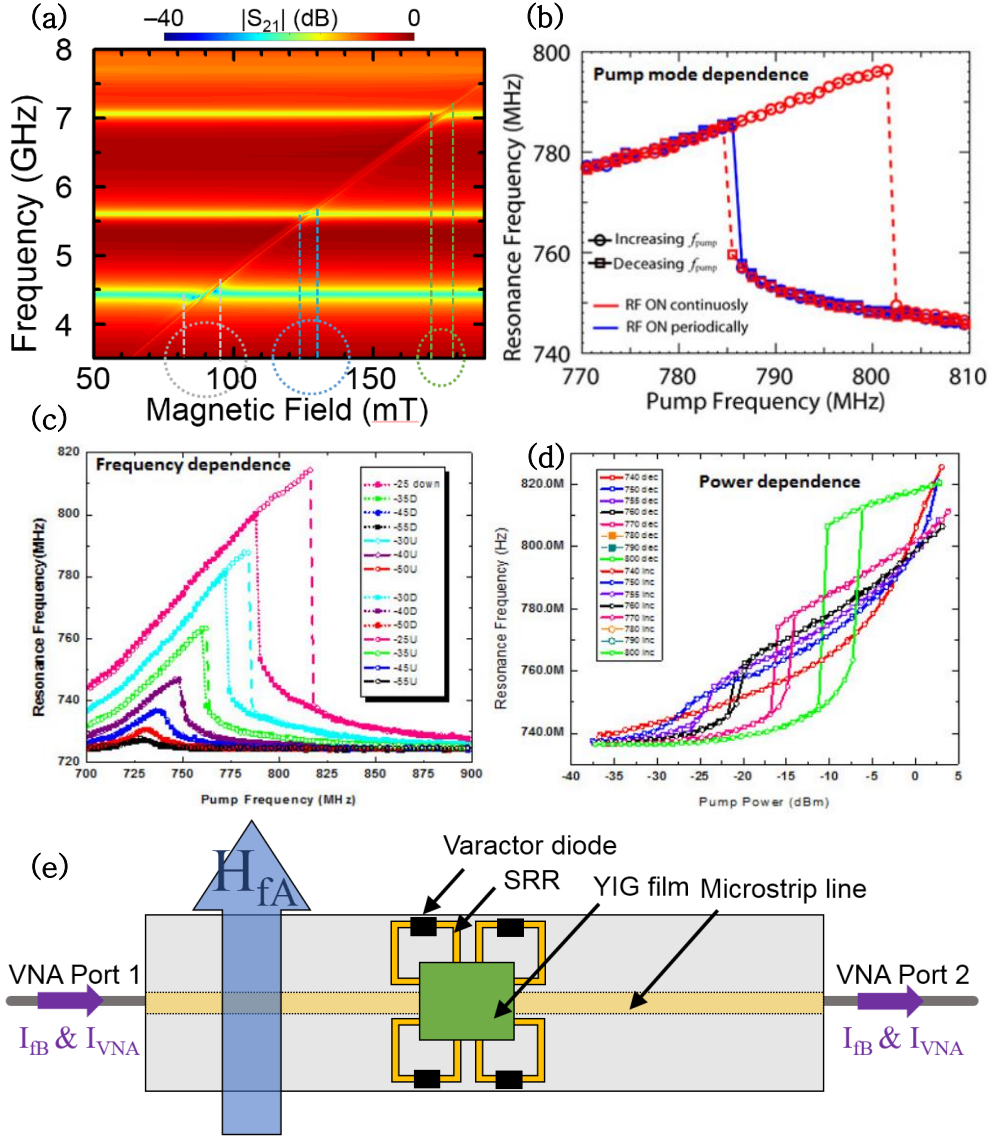
Figure 67. (a) Illustration of the coupling states and the coupling ranges in a three ISRRs sample. Grey, blue, and green lines and circle show the coupling ranges in Ampere of each ISRR. (b) Pump power dependence of a v−SRR resonance frequency to a continuously or periodically applied pump. (c) Frequency and (d) Pump dependence of a v−SRR resonance frequency. [92] (e) Schematic of the suggested experimental setup illustrated with 4 v−SRRs. Varactors voltage sources are not shown.

90

Chapter 6. Conclusion

Neuromorphic computing using photon−magnon coupling in an ISRR/YIG hybrid system was successfully experimentally demonstrated. Using the reservoir computing paradigm, non−degenerate waveforms classification was performed using the frequency, S_{21} magnitude and phase of the coupled mode. Perfect success rates were obtained from each neuron function. with vast regions of perfect success rates from both the S_{21} and frequency functions and three points of perfect rate from the phase function (figure 31).

Additionally, experimental success rates from the frequency function for two YIG film positions confirm the predicted performance increase owed to higher coupling strengths (figure 19 and figure 32). Results can be compared with reference [28] shown in figures 2 and 3. The hybrid system leads to broad regions of perfect success rate while success rates obtained from an STNO do not reach 100% and show only one to two smaller peaks of high performances.

This thesis also shows a reliable simulation method to predict experimental performances. The expected results of various

systems and configurations were obtained by putting measured or theoretical neuron functions into the LabVIEW code. The simulation showed the superiority of the ISRR/YIG coupled system on the ISRR or YIG alone. Being almost constant, neuron functions from the ISRR naturally lead to random or low success rates (figure 14). On the other hand, the classification task can be successfully performed using the magnon frequency function, as shown by wide peaks of perfect success rates in figure 16. While the peaks tend to increase in length as the spin-wave mode gets lower, the maximum NSE is independent of the mode order and lower than the NSE obtained from the coupled-mode frequency function, thus justifying the superiority of the CMP frequency function over the magnons frequency function.

The two main limitations of the current system are the magnetic field time delay and the absence of both intrinsic and extrinsic memory. The time delay limits the usage of a large data set and neuron number, while the lack of memory limits the number of tasks to perform. Both limitations could be overcome by using transient dynamics of photon-magnon coupling [83]. In such a two-state system (the coupled mode is made up of a photon and magnon state), Rabi-oscillations can be observed as a response to

microwave current pulse excitations applied to either or both the cavity and the magnon source. Inputs would be encoded in the nanosecond to microsecond pulse amplitude or frequency. At the same time, the output would be the amplitude or frequency of Rabi−oscillations red from nanosecond time−resolved measurement techniques [84]. The intrinsic memory would come from the Rabi−oscillation damping, while a feedback delay line could create the extrinsic memory as in ref [28]. Implementing single node reservoir computing would tremendously speed up the computation by exploiting the time scale associated with the coupling strength.

An intermediate step would be to stay in the steady−state dynamics but in the non−linear regime. Inputs would be encoded in the pump power or frequency, and the neuron output would be the frequency of the upper or lower CMP since the frequency in the non−linear regime is a non−linear function [85]. This concept allows the implementation of a feedback loop but does not implement an intrinsic memory.

Finally, the concept of vowel recognition using photon−magnon coupling in a varactor−loaded SRR array has been presented, and a solution for encoding the second frequency coordinate f_B

suggested. Besides pursuing this work, an interesting additional experiment will be to study the non−linear regime of a PM coupled v−SRR since both a PM coupled system and a v−SRR independently exhibit bistability [93].

References

[1] G. E. Moore, ''Cramming more components onto integrated circuits", *Electronics*, vol. 38, no. 8, pp. 114−117, 1965.

[2] G. E. Moore, "Progress In Digital Integrated Electronics", *IEDM Tech. Digest,* vol. 21 pp. 11−13, 1975.

[3] P. Gargini," The International Technology for Semiconductors (ITRS)："Past, Present and Future*""*, *IEEE GaAs IC Symposium*, 22nd Annual Technical Digest 2000, pp. 3−5, 2000.

[4] E. Pop, S. Sinha and K. E. Goodson, "Heat Generation and Transport in Nanometer−Scale Transistors", *Proceedings of the IEEE*, vol. 94, no. 8, pp. 1587−1601, 2006.

[5] S. H. Fuller and L. I. Millett, "The Future of Computing Performance: Game Over or Next Level?", Washington, DC: The National Academies Press, 2011.

[6] M. M. Waldrop, "The chips are down for Moore's law", *Nature*, vol. 530, no. 7589, pp. 144−147, 2016.

[7] A. M. Turing, "Computing Machinery and Intelligence", *Mind*, vol. 59, no. 236, pp. 433−460, 1950.

[8] C. D. James, J. B. Aimone, N. E. Miner, C. M. Vineyard, F. H. Rothganger, K. D. Carlson, S. A. Mulder, T. J. Draelos, A. Faust, M. J. Marinella, J. H. Naegle, S. J. Plimpton, "A historical survey of algorithms and hardware architectures for neural−inspired and

neuromorphic computing applications", *Biologically Inspired Cognitive Architectures,* vol. 19, pp 49－64, 2017.

[9] C. Mead, "Analog VLSI and Neural Systems", MA, USA: Addison－Wesley, 1989.

[10] A. Calimera, E. Macii, and M. Poncino, "The Human Brain Project and neuromorphic computing", *Functional Neurology,* vol. 28, no. 3, pp. 191－196, 2013.

[11] S. Ackerman, "Discovering the Brain", Washington (DC): National Academies Press (US), 1992.

[12] JG. Barbara, "Les heures sombres de la Neurophysiologie a Paris (1909–1939)", *La Lettre des Neurosciences*, vol. 29, pp. 3–6, 2005.

[13] B. W. Knight, "Dynamics of encoding in a population of neurons", *J. Gen. Physiol.,* vol. 59, no. 6, pp. 734－766, 1972.

[14] R. Stein, "A theoretical analysis of neuronal variability", *Biophys. J.,* vol. 5, no. 2, pp. 173–194, 1965.

[15] N. Brunnel, M. C.W. van Rossum, "Lapicque's 1907 paper: from frogs to integrate－and－fire", *Biological Cybernetics*, vol. 97, pp. 337–339, 2007.

[16] J. Zhu, T. Zhang, Y. Yang, and R. Huang, "A comprehensive review on emerging artificial neuromorphic devices", *Appl. Phys. Rev.*, vol. 7, no. 1, 011312, 2020.

[17] E. R. Kandel, J. H. Schwartz, T. M. Jessell, S. A. Siegelbaum,

and A. J. Hudspeth, "Principles of Neural Science", 5th ed. McGraw-Hill, New York, USA, 2013.

[18] G.-Q. Bi and M.-M. Poo, "Synaptic Modifications in Cultured Hippocampal Neurons: Dependence on Spike Timing, Synaptic Strength, and Postsynaptic Cell Type", *J. Neurosci.*, vol. 18, no. 24, pp.10464-10472 (1998).

[19] G. Rachmuth, Z. Shouval, M. Bear and C.-S. Poon, "A biophysically-based neuromorphic model of spike rate- and timing-dependent plasticity", *Proc. Nat. Acad. Sci. U. S. A.*, vol. 108, no. 49, pp. 1266-1277, 2011.

[20] D. Ielmini, "Resistive switching memories based on metal oxides: mechanisms, reliability and scaling", *Semicond. Sci. Technol.*, vol 31, no.6, 063002, 2016.

[21] P. Junsangsri, F. Lombardi and J. Han, "Macromodeling a phase change memory (PCM) cell by HSPICE," *Proceedings of the 2012 IEEE/ACM International Symposium on Nanoscale Architectures*, pp. 77–84, 2012.

[22] A. Chanthbouala, V. Garcia, R. O. Cherifi, K. Bouzehouane, S. Fusil, X. Moya, S. Xavier, H. Yamada, C. Deranlot, N. D. Mathur, M. Bibes, A. Barthelemy and J. Grollier, "A ferroelectric memristor", *Nat. Mater.*, vol. 11, pp. 860-864, 2012.

[23] J. Grollier, D. Querlioz, K. Y. Camsari, et al, "Neuromorphic spintronics", *Nat. Electron.*, vol.3, pp. 360–370, 2020.

[24] Y. Zhang, Z. Wang, J. Zhu, Y. Yang, M. Rao, W. Song, Y. Zhuo, X. Zhang, M. Cui, L. Shen, R. Huang and J. J. Yang, "Brain-inspired computing with memristors: Challenges in devices, circuits, and systems", *Appl. Phys. Rev.*, vol. 7, 011308, 2020.

[25] H. Wu, P. Yao, B. Gao, et al., "Multiplication on the edge", *Nat. Electron.,* vol 1, pp. 8–9, 2018.

[26] J. Torrejon, M. Riou, F. Araujo, et al., "Neuromorphic computing with nanoscale spintronic oscillators", *Nature*, vol. 547, pp. 428–431, 2017.

[27] M. Romera, P. Talatchian, S. Tsunegi, et al., "Vowel recognition with four coupled spin-torque nano-oscillators", *Nature*, vol. 563, pp. 230–234, 2018.

[28] D. Marković, N. Leroux, M. Riou, F. Abreu Araujo, J. Torrejon, D. Querlioz, A. Fukushima, S. Yuasa, J. Trastoy, P. Bortolotti and J. Grollier, "Reservoir computing with the frequency, phase, and amplitude of spin-torque nanooscillators", *Appl. Phys. Lett.*, vol. 114, 012409, 2019.

[29] M. Riou, J. Torrejon, B. Garitaine, F. Abreu Araujo, P. Bortolotti, V. Cros, S. Tsunegi, K. Yakushiji, A. Fukushima, H. Kubota, S. Yuasa, D. Querlioz, M. D. Stiles, and J. Grollier, "Temporal Pattern Recognition with Delayed-Feedback Spin-Torque Nano-Oscillators", *Phys. Rev. Applied*, vol. 12, no. 2, 024049, 2019.

[30] T. Kanao, H. Suto, K. Mizushima, H. Goto, T. Tanamoto and T. Nagasawa, "Reservoir Computing on Spin－Torque Oscillator Array", *Phys. Rev. Applied*, vol. 12, no. 2, 024052, 2019.

[31] B. Bhoi and S. K. Kim, "Photon－magnon coupling: Historical perspective, status, and future directions", *Solid State Physics*, vol. 70, 2019.

[32] B. Bhoi and S. K. Kim, "Roadmap for photon－magnon coupling and its applications", *Solid State Physics*, vol. 71, 2020.

[33] J. J. Hopfield, "Theory of the contribution of excitons to the complex dielectric constant of crystals", *Phys. Rev.*, vol. 112, no. 5, pp. 1555－1567, 1958.

[34] H. Kun, "Lattice vibrations and optical waves in ionic crystals", *Nature*, vol. 167, no. 4254, pp. 779–780, 1951.

[35] R. J. Thompson, G. Rempe, and H. J. Kimble, "Observation of normal－mode splitting for an atom in an optical cavity", *Phys. Rev. Lett.*, vol. 68, no. 8, pp. 1132－1135, 1992.

[36] J. J. Childs, K. An, M. S. Otteson, R. R. Dasari and M.S. Feld, "Normal－Mode Line Shapes for Atoms in Standing－Wave Optical Resonators", *Phys. Rev. Lett.*, vol. 77, no 14, pp. 2901－2904, 1996.

[37] G. Kurizki, P. Bertet, Y. Kubo, K. Mølmer, D. Petrosyan, P. Rabl and J. Schmiedmayer, "Quantum technologies with hybrid systems", *Proc. Nat. Acad. Sci. U. S. A.*, vol. 112, no. 13, pp. 3866－3873, 2015.

[38] C. Weisbuch, M. Nishioka, A. Ishikawa, and Y. Arakawa, "Observation of the coupled exciton－photon mode splitting in a

semiconductor quantum microcavity", *Phys. Rev. Lett.*, vol. 69, no. 23, pp. 3314−3317, 1992.

[39] J. Fink, M. Göppl, M. Baur, et al., "Climbing the Jaynes–Cummings ladder and observing its non−linearity in a cavity QED system", *Nature,* vol. 454, pp. 315–318, 2008.

[40] S. Haroche, "Nobel Lecture: Controlling photons in a box and exploring the quantum to classical boundary", *Rev. Mod. Phys.*, vol. 85, no. 3, pp. 1083−1102, 2013.

[41] O. O. Soykal and M. E. Flatte, "Strong field interactions between a nanomagnet and a photonic cavity", *Phys. Rev. Lett.*, vol. 104, no. 7, 077202, 2010.

[42] H. Huebl, C. W. Zollitsch, J. Lotze, F. Hocke, M. Greifenstein, A. Marx, R. Gross, and S. T. B. Goennenwein, "High cooperativity in coupled microwave resonator ferrimagnetic insulator hybrids" *Phys. Rev. Lett.*, vol. 111, no. 12, 127003, 2013.

[43] X. Zhang, C. L. Zou, L. Jiang, and H. X. Tang, "Strongly Coupled Magnons and Cavity Microwave Photons", *Phys. Rev. Lett.*, vol. 113, no. 15, 156401, 2014.

[44] M. Harder, L. Bai, C. Match, J. Sirker, and C. M. Hu, "Study of the cavity−magnon−polariton transmission line shape", *Sci. China−Phys. Mech. Astron.,* vol. 59, no. 11, 117511, 2016.

[45] B. Bhoi, K. Bosung, J. Seung−Hun, J. Kim, J. Yang, Y. J. Cho and S.K. Kim, "Abnormal anti−crossing effect in photon−magnon coupling", *Phys. Rev. B*, vol. 99, no. 13, 134426, 2019.

[46] G. B. G. Stenning, G. J. Bowden, L. C. Maple, S. A. Gregory, A. Sposito, R. W. Eason, N. I. Zheludev, and P. A. J. de Groot, "Magnetic control of a meta-molecule," *Opt. Express*, vol. 21, no. 2, pp. 1456-1464, 2013.

[47] B. Bhoi, T. Cliff, I. S. Maksymov, M. Kostylev, R. Aiyar, N. Venkataramani, S. Prasad, and R. L. Stamps, "Study of photon-magnon coupling in a YIG-film split-ring resonant system", *J. Appl. Phys.*, vol. 116, no. 24, 243906, 2014.

[48] B. Bhoi, B. Kim, J. Kim, Y. J. Cho, and S.K. Kim, "Robust magnon-photon coupling in a planar-geometry hybrid of inverted split-ring resonator and YIG film", *Sci. Rep.,* vol. 7, 11930, 2017.

[49] R. J. Schoelkopf and S. M. Girvin, "Wiring up quantum systems", *Nature*, vol. 451, pp. 664-669, 2008.

[50] H. Kimble, "The quantum internet", *Nature*, vol. 453, pp. 1023–1030, 2008.

[51] Y. Tabuchi, S. Ishino, A. Noguchi, T. Ishikawa, R. Yamazaki, K. Usami, and Y. Nakamura, "Coherent coupling between a ferromagnetic magnon and a superconducting qubit", *Science*, vol. 349, no. 6246, pp. 405-408, 2015.

[52] X. F. Zhang, C. L. Zou, N. Zhu, F. Marquardt, L. Jiang and H. X. Tang, "Magnon dark modes and gradient memory", *Nat. Commun.*, vol. 6, 8914, 2015.

[53] Y. Li, W. Zhang, V. Tyberkevych, W.K. Kwok, A. Hoffmann, and V. Novosad, "Hybrid magnonics: Physics, circuits, and applications

for coherent information processing", *J. Appl. Phys.*, vol. 128, no. 13, 130902, 2020.

[54] D. P. Mandic, J. A. Chambers, et al., "Recurrent neural networks for prediction: learning algorithms, architectures and stability", Wiley Online Library, 2001.

[55] G. Tanaka, T. Yamane, J. B. Héroux, R. Nakane, N Kanazawa, S Takeda, H. Numata, D. Nakano, and A. Hirose, "Recent advances in physical reservoir computing: A review", *Neural Networks*, vol. 115, pp 100−123, 2019.

[56] H. Jaeger, "The "echo state" approach to analysing and training recurrent neural networks. *GMD Report 148*, German National Research Center for Information Technology, 2001.

[57] L.Appeltant, M. Soriano, G. Van der Sande, et al., "Information processing using a single dynamical node as complex system", *Nat. commun.,* vol. 2, no. 468, 2011.

[58] L. Appeltant, G. Van der Sande, J. Danckaert and I. Fischer, "Constructing optimized binary masks for reservoir computing with delay systems", *Sci. Rep.*, vol. 4, no. 3629, 2014.

[59] Y. Paquot, F. Duport, A. Smerieri, J. Dambre, B. Schrauwen, M. Haelterman and S. Massar, "Optoelectronic reservoir computing", *Sci. Rep.*, vol. 2, no. 287, 2012.

Hardware implementation of single node RC has been demonstrated with electrical systems [57],[59], mechanical systems [60]−[61], photonic systems [62]−[68], memristor array [69] and spintronics

using STNOs [26]−[30], [70]. Waveform recognition of a degenerate [28] or non−degenerate [59] sequence is a typical benchmark task for RC with a single hardware node. Non−degenerate waveform recognition is the task performed in this thesis.

[60] K. Caluwaerts, M. D'Haene, D. Verstraeten and B. Schrauwen, "Locomotion without a brain: Physical reservoir computing in tensegrity structures," *Artif. Life* , vol. 19, no. 1, pp. 35–66, 2013.

[61] G. Dion, S. Mejaouri and J. Sylvestrea, "Reservoir computing with a single delay−coupled non−linear mechanical oscillator featured", *J. Appl. Phys.*, vol. 124, no. 15, 152132, 2018.

[62] K. Vandoorne, P. Mechet, T. Van Vaerenbergh, M. Fiers, G. Morthier, D. Verstraeten, B. Schrauwen, J. Dambre, and P. Bienstman, "Experimental demonstration of reservoir computing on a silicon photonics chip," *Nat. Commun.*, vol. 5, no. 3541, 2014.

[63] D. Brunner, M. C. Soriano, C. R. Mirasso, and I. Fischer, "Parallel photonic information processing at gigabyte per second data rates using transient states", *Nat. Commun.*, vol. 4, no. 1364, 2013.

[64] A. Dejonckheere, F. Duport, A. Smerieri, L. Fang, J.−L. Oudar, M. Haelterman, and S. Massar, "All−optical reservoir computer based on saturation of absorption", *Opt. Express*, vol. 22, no. 9, pp. 10868− 10881, 2014.

[65] F. Duport, A. Smerieri, A. Akrout, M. Haelterman, and S. Massar, "Fully analogue photonic reservoir computer", *Sci. Rep.*, vol. 6, no. 22381, 2016.

[66] Q. Vinckier, F. Duport, A. Smerieri, K. Vandoorne, P. Bienstman, M. Haelterman, and S. Massar, "High−performance photonic reservoir computer based on a coherently driven passive cavity", *Optica*, vol. 2, no. 5, pp. 438−446, 2015.

[67] F. Duport, B. Schneider, A. Smerieri, M. Haelterman, and S. Massar, "All−optical reservoir computing", *Opt. Express*, vol. 20, no. 20, pp. 22783−22795, 2012.

[68] K. Vandoorne, W. Dierckx, B. Schrauwen, D. Verstraeten, R. Baets, P. Bienstman, and J. V. Campenhout, "Toward optical signal processing using Photonic Reservoir Computing", *Opt. Express*, vol. 16, no. 15, pp. 11182−11192, 2008.

[69] C. Du, F. Cai, M. A. Zidan, W. Ma, S. H. Lee, and W. D. Lu, "Reservoir computing using dynamic memristors for temporal information processing," *Nat. Commun.*, vol. 8, no. 2204, 2017.

[70] S. Tsunegi, T. Taniguchi, K. Nakajima, S. Miwa, K. Yakushiji, A. Fukushima, S. Yuasa, and H. Kubota, "Physical reservoir computing based on spin torque oscillator with forced synchronization", *Appl. Phys. Lett.,* vol. 114, no. 16, 164101, 2019.

[71] H. V. Gupta, and H. Kling, "On typical range, sensitivity, and normalization of Mean Squared Error and Nash−Sutcliffe Efficiency type metrics", *Water Resour. Res.*, vol. 47, no. 10, W10601, 2011.

[72] B. D. Cullity, and C. D. Graham, "Introduction to Magnetic Materials", Wiley−IEEE Press, 2008.

[73] T.L. Gilbert, "A phenomenological theory of damping in ferromagnetic materials", *IEEE Trans. Magn.*, vol. 40, no. 6, pp. 3443-3449, 2004.

[74] D.D. Stancil, and A. Prabhakar, "Spin Waves: Theory and Applications", Springer US, 2009.

[75] X. Zhang, C. Zou, L. Jiang, and H.X. Tang, "Superstrong coupling of thin film magnetostatic waves with microwave cavity", *J. Appl. Phys.*, vol. 119, no .2, 023905, 2016.

[76] J.B. Pendry, A.J. Holden, D.J. Robbins, W.J. Stewart, "Magnetism from conductors and enhanced non-linear phenomena", *IEEE Trans. Microwave Theory Tech.,* vol. 47, no. 11, pp. 2075–2084, 1999.

[77] F. Falcone, T. Lopetegi, J. D. Baena, R. Marqués, F. Martín, and M. Sorolla, "Effective negative-ϵ stop-band microstrip lines based on complementary split ring resonators," *IEEE Microw. Wireless Compon. Lett.*, vol. 14, no. 6, pp. 280–282, 2004.

[78] D. M. Pozar, "Microwave Engineering 3rd Ed.", Wiley, New York, 2005.

[79] D. R. Smith, W. J. Padilla, D. C. Vier, S.C. Nemat-Nasser, and S. Schultz, "Composite medium with simultaneously negative permeability and permittivity", *Phys. Rev. Lett.*, vol. 84, no. 18, pp. 4184-4187, 2000.

[80] M. Sparks, "Ferromagnetic-Relaxation Theory," M-Hill, 1964.

[81] W.T. Soh, B. Peng, C.K. Ong, "Localized excitation of magnetostatic surface spin waves in yttrium iron garnet by shorted coaxial probe detected via spin pumping and rectification effect", *J. Appl. Phys.,* vol. 117, no. 15, 153903, 2015.

[82] B. Kim, B. Bhoi, S. K. Kim, "Spin-wave excitation and critical angles in a hybrid photon-magnon-coupled system", *J. Appl. Phys.*, vol. 126, no. 16, 163902, 2019.

[83] C. Match, M. Harder, L. Bai, P. Hyde, C. M. Hu, "Transient response of the cavity magnon-polariton", *Phys. Rev. B.,* vol. 99, no. 13, 134445, 2019.

[84] T. Wolz, A. Stehli, A.Schneider, et al., "Introducing coherent time control to cavity magnon-polariton modes", *Commun. Phys.*, vol. 3, no. 3, 2020.

[85] Y. P Wang, G. Q. Zhang, D. Zhang, L. Dengke, T. F. Li, C.-M. Hu, J. Q. You, "Bistability of Cavity Magnon Polaritons", *Phys. Rev. Lett.*, vol. 120, no. 5, 057202, 2018.

[86] P. Talatchian *et al.*, "Microwave Neural Processing and Broadcasting with Spintronic Nano-Oscillators," *2018 IEEE International Electron Devices Meeting (IEDM)*, San Francisco, CA, pp. 27.4.1-27.4.4, 2018.

[87] T. Chen *et al.*, "Spin-Torque and Spin-Hall Nano-Oscillators," *Proceedings of the IEEE*, vol. 104, no. 10, pp. 1919-1945, 2016.

[88] A. Slavin and V. Tiberkevich, "Nonlinear Auto-Oscillator Theory of Microwave Generation by Spin-Polarized Current", *IEEE transactions on magnetics*, vol. 45, no. 4, 2009.

[89] S. Kaur, B. M. Yao, J. W. Rao, Y. S. Gui, and C.-M. Hu, "Voltage control of cavity magnon polariton", *Appl. Phys. Lett.,* vol. 109, no. 3, pp. 032404, 2016.

[90] B. Wang, J. Zhou, T. Koschny, C. M. Soukoulis, "Non-linear properties of split-ring resonators", *Opt. Express*, vol. 16, no. 20, pp. 16058

[91] I. V. Shadrivov, S. K. Morrison, and Yuri S. Kivshar, "Tunable split-ring resonators for non-linear negative-index metamaterials", *Opt. Express*, vol. 14, no. 20, pp. 9344-9349, 2006.

[92] S. R. Silva, A. D. Shields, and J. Zhou, "Tunable Optical Bistability and Optical Switching by Nonlinear Metamaterials", arXiv:1607.1705[physics.app-ph].

[93] Y.F Wang, G.Q Zhang, D. Zhang, T.F Li, C.-M. Hu and, J. Q. You, "Bistability of Cavity Magnon Polaritons", *Phys. Rev. Lett.,* vol. 120, no. 5, pp. 057202, 2018.

초록

Loïc Millet

서울대학교 재료공학부 대학원

뉴로모픽 컴퓨팅은 작업을 수행함에 있어서 기존 컴퓨팅을 능가할 수 있도록 인간의 두뇌를 기반으로 설계된 컴퓨팅 패러다임입니다. 특히 저장소(Reservoir) 컴퓨팅은 뉴로모픽 컴퓨팅의 한 형태로서 작업을 수행하기 위해서 저장소라고 하는 비선형 뉴런들이 반복적이고 무작위로 상호 연결되어 있는 네트워크를 사용합니다. 뉴로모픽 컴퓨팅의 효율을 증대시키기 위하여 스핀트로닉스에 기반하여 뉴로모픽 컴퓨팅을 구현하는 연구들이 활발히 진행되고 있습니다. 기존 CMOS 시스템은 뉴런과 시냅스의 특성 자체를 모방하려 하는 반면에, 뉴로모픽 장치에 대한 연구는 본질적으로 두뇌 자체와 유사한 장치를 만드는 것을 목표로 하고 있습니다.

본 연구에서 우리는 2D 하이브리드 구조에서의 광-마그논 상호작용을 사용하여 뉴런을 구현함으로써 Reservoir 컴퓨팅 패러다임에서의 파형 인식을 성공적으로 수행하였습니다. 2D 하이브리드 시스템은 ISRR(Inverted Split-Ring Resonator, 반전된 분할 링 공진기)과 YIG(Yttrium Iron Garnet) 박막으로 구성됩니다. 광자-마그논 결합 혹은 CMP(Cavity-Magnon Polariton)이라 불리는 이

모드의 속성을 파형이 균일한 정자기장의 형태로 입력되는 동안 뉴런의 출력으로써 이용하였습니다. 광-마그논 상호작용의 공진주파수, S21 파라미터의 매개 변수 크기 및 위상으로 얻은 높은 실험적 성공률은 뉴로모픽 시스템에서의 분류 작업에 대한 광-마그논 결합의 유용성을 처음으로 제시하였습니다. 본 연구는 2D 하이브리드 시스템에서 광-마그논 결합을 사용한 더 고차원적인 작업과 뉴로모픽 네트워크를 구현하기 위한 첫 번째 단계라고 할 수 있습니다. 이는 더 나아가 뉴로모픽 컴퓨팅 체계에 기반한 다음 단계의 시스템의 개념을 제시합니다. STNO(Spin Torque Nano-Oscillator)을 사용한 선행 연구에서 입증된 바와 같이, 뉴런 집합을 모방한 공진기 배열과 입력 신호를 받아들이는 외부 주파수 간의 동기화를 통하여 생체의 연산과 유사한 컴퓨팅 시스템을 구현할 수 있습니다. 이러한 개념은 모음 인식을 수행하기 위하여 사용되었으며, 본 연구진은 광자-마그논 결합을 이용하여 해당 개념을 구현할 계획입니다.

Acknowledgment

Firstly, I want to express my gratitude to Professor Sang−Koog Kim, my advisor, for the opportunity to research in two emerging and exciting fields, namely photon−magnon coupling and neuromorphic computing. His insights, trust, and encouragement made my master thesis in Korea an enjoyable experience.

I would like to thank all the Nanospinics Laboratory members. Dr. Biswanath Bhoi, Bosung Kim, and Haechan Jeon for their continuous support during my research work. Jaehak Yang, Jae Hyeok Lee, Yongsub Kim, Jaegun Sim, Hyeon−Kyu Park, Gyu Young Park, Inna Yusnila Khairani, Trivoramai Jilalerspong, Anindityo Nugra Arifiadi, Jiyeol Yoon, Ahn Hyeon, Seung−hoon Jang, and Yeonjoo Oh for their help, time, and the friendly discussions we could have. My thoughts are also going to the friends I made in and outside the university, who made my two years in Korea a memorable experience in my life.

Finally, I would like to express my deepest gratitude to my family for their support and trust. I would not be here without you.